

**PREDICTING IN-PLANE UNIAXIAL COMPRESSIVE MODULI OF
HEXAGONAL HONEYCOMBS USING EXPERIMENTAL ANALOGUES**

by

BARIŞ EMRE KIRAL

Submitted to the Graduate School of Engineering and Natural Sciences

in partial fulfillment of

the requirements for


the degree of Master of Science

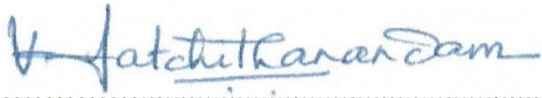
Sabanci University

August 2020

PREDICTING IN-PLANE UNIAXIAL COMPRESSIVE MODULI OF
HEXAGONAL HONEYCOMBS USING EXPERIMENTAL ANALOGUES

APPROVED BY:

Prof. Dr. Melih Papila (Thesis Supervisor):.....

Prof. Dr. Satchi Venkataraman:.....

Prof. Dr. Ali Rana Atılgan:.....

DATE OF APPROVAL: 01/09/2020

© Barış Emre Kırал 2020

All Rights Reserved

To my family...

Predicting In-Plane Uniaxial Compressive Moduli of Hexagonal Honeycombs Using Experimental Analogues

Bariş Emre Kiral

Material Science and Nanoengineering

Master of Science Thesis, 2020

Thesis Advisor: Prof. Dr. Melih Papila

Keywords: 2D honeycombs, unit cells, effective modulus prediction, finite element analysis, mechanical testing, experimental analogues

Abstract

Cellular solids have been utilized in many engineering applications for thermal insulation, their high specific out-of-plane compressive strengths and stiffnesses, their sieving capabilities, and in-plane energy absorption properties. With the advances in additive manufacturing, numerous novel 2D cellular solid designs have emerged. In-plane properties of 2D cellular solids have attracted attention for their intriguing behaviour under compressive, tensional and shear loads.

As structures deviate from common geometries such as square, triangular, or hexagonal, analytical and numerical methods to predict effective elastic properties get dramatically more convoluted. Thus, analytical models in particular have been limited to the simpler designs. Moreover, validating and/or characterizing experimental analyses of novel geometries are often limited in scope due to size effects and inconsistent constraints among the test specimens and practical structures.

This study presents a new approach that amalgamates virtual and real-life static analysis of cellular structures of repeating cells. Representative equivalent structures for testing, i.e. analogue test specimens are determined using parametric FEM analysis. Analogues for hexagonal honeycomb arrays are manufactured and tested under compression. Compressive moduli of the selected analogues exhibit great consistency between numerical and experimental analyses. The approach sets a framework for future research in using analogues for determination of in-plane properties of numerous other 2D cellular solid designs.

Deneyisel Analoglar Kullanılarak Altıgen Bal Peteđi Yapıların Düzlem İçi Tek Eksenli Basma Modülünün Belirlenmesi

Bariş Emre Kıral

Malzeme Bilimi ve Nanomühendislik

Yüksek Lisans Tezi, 2020

Tez Danışmanı: Prof. Dr. Melih Papila

Anahtar Kelimeler: 2B hücreli katılar, birim hücreler, etkin elastisite modülü öngörüsü, sonlu ögeli çözümleme, mekanik testler, deneysel analog yapılar

Özet

Hücreli katı malzemeler, ısı yalıtımı, yüksek düzlem dışı bükülmezlik ve mukavemeti, eleme özelliđi ve düzlem içi ve dışı enerji emme kapasitesi nedeniyle pek çok mühendislik alanında kullanılmaktadır. Eklemeli üretimdeki gelişmeler ile pek çok özgün iki boyutlu (2B) hücreli yapı tasarımı ortaya çıkmıştır. 2B hücreli katıların basma, çekme ve kesme altındaki davranışı özellikle ilgi çekmektedir.

Yapılar kare, üçgen, altıgen gibi alışılmış yapılardan uzaklaştıkça etkin elastik özelliklerin analitik ve denerik yöntemlerle öngörülmesi çarpıcı biçimde karışık bir hal almaktadır. Bu nedenle, özellikle analitik çözümler daha basit şekillerle sınırlı kalmıştır. Buna ek olarak özgün şekilleri nitelendirmek ve/veya doğrulamak için yapılan deneysel testler, boyut etkileri ve deney-gerçek yapı arasındaki tutarsız kısıtlama koşulları nedeni ile sınırlı bir şekilde yapılabilmektedir.

Bu çalışma tekrarlayan 2B hücreli yapıların denenmesi için zahiri ve gerçek durađan çözümlemeyi birleştiren bir yaklaşım sunmaktadır. Fiziksel test için temsili eşdeđer aday yapılar önerilmiş ve sonlu elemanlar çözümleme yöntemi ile sanal olarak tasarlanmış ve tekrarlayan referans yapı sonuçlarına göre sınanmıştır. Bu deneysel analog yapılar daha sonra üretilmiş ve basma altında test edilmiştir. Seçilen analog yapıların basma modülleri denerik ve deneysel çözümlemeler arasında tutarlılık göstermiştir. Bu yaklaşım ile, gelecekte pek çok diđer hücreli yapıların özelliklerinin deneysel analoglar kullanılarak belirlenmesi için bir çerçeve ortaya konulmuştur.

Acknowledgements

I would like to thank my thesis advisor and dear mentor, Prof. Dr. Melih Papila for his guidance, support, and most importantly his unending intrigue that never failed to motivate me.

I would like to thank my thesis jury members, Prof. Dr. Ali Rana Atilgan and Prof. Dr. Satchi Venkataraman for their comments and insight regarding this work.

I would like to thank my mother, Dr. Asuman Kırıl and my father, Prof. Dr. Ahmet Kırıl and for decades of love, support, understanding and most importantly patience when I was nothing short of difficult. I would not be where I am without them.

I would like to thank my brother, Murat Can Kırıl, for his support and friendship through thick and thin.

Even though she will never understand this, I am thankful for my dog Kali who never left my side and constantly distracted me with her cute snoring when writing this thesis.

I would like to thank my beloved Melike Nur Önder, who, with her affection and support, made graduate school the best years of my life.

Lastly, I would like to thank Sabanci University Materials Science family for all the great years we have spent together, doing what we love most.

Table of Contents

1	Introduction.....	1
1.1	General Introduction.....	1
1.2	Analytical Models for Calculating Effective Modulus	3
1.3	Refining the Analytical Model.....	6
1.4	Limitations of Analytical and Experimental Models.....	8
1.4.1	Geometric Changes in Stiffness	8
1.4.2	Isotropic Assumption.....	9
1.4.3	Size Effect	10
1.5	Research Hypothesis.....	11
2	Methods.....	12
2.1	Representative Element and Reference Array Design	12
2.2	Finite Element Analysis.....	17
2.3	Design and 3D Printing of Specimens	20
2.4	Mechanical testing	21
3	Results & Discussion.....	23
3.1	FEA Results	23
3.1.1	Naming Convention	23
3.1.2	List of Virtual Test Specimens.....	24
3.1.3	Reference Array Simulations.....	25
3.1.4	Representative Element Simulations	27
3.1.4.1	RE-α Simulations.....	27
3.1.4.2	RE-β Simulations.....	30
3.1.4.3	RE-γ simulations.....	33
3.1.5	Representative Ratio for Analogous Specimens	36
3.2	Mechanical Testing Results.....	40
3.3	Choosing the Most Applicable Geometry	42

3.3.1	Consistency of Response.....	42
3.3.2	Scalability of Response	43
3.3.3	Range of Application	44
3.4	Data Fitting for Determination of b_t for Target Relative Densities.....	44
3.4.1	Data Fitting Example Case	46
3.5	Future Work.....	47
4	Conclusion	48
5	References.....	49

List of Figures

Figure 1. Behavior of honeycombs under in-plane compression (Adapted from Ashby; Gibson; ‘<i>Cellular Solids</i>’ 1997)	2
Figure 2. Dimensions and orientations in a regular hexagonal unit cell.	3
Figure 3. Forces and moments acting on inclined members under compression in the 1-direction (a) and 2-direction (b).....	3
Figure 4. Deflection of inclined member represented as the sum of deflections from axial, shear and bending loads.....	7
Figure 5. Change in dimensions and orientations of load-carrying members causing a change in effective stiffness.	8
Figure 6. Different shapes of honeycombs with equally dimensioned unit cells. Different boundary conditions result in different moduli.....	10
Figure 7. W and D lengths in size parameter ‘α’.	11
Figure 8. Flowchart summarizing research steps.	11
Figure 9. RVE’s under periodic boundary conditions from various research *	12
Figure 10. Deformation of an isolated unit cell under compression.	13
Figure 11. Deformation of a central cell within the array.	13
Figure 12. Transverse directional deformation of an array under compression in the 2-direction (y-axis in the image). Note that the central array experiences no transverse deformation and the edges show maximum transverse deformation (red and dark blue)	14
Figure 13. The spider-web structure and the constraints imposed on these structures by an enclosed shell.	15
Figure 14. Dimensions of RA (top-left), RE-α (top-right), RE-β (bottom-left) and RE-γ (bottom-right) for FEM and experimental analysis.....	16
Figure 15. Mechanical tests of PLA for modulus determination.	17
Figure 16. Typical mesh applied to specimens (left) and a specimen under deformation showing maximum principal stress (right).....	18
Figure 17. Flowchart for FEM analysis	19

Figure 18. Flowchart for FDM manufacturing.....	20
Figure 19. Schematic of the compression jig.	21
Figure 20. Testing setup (left), 3D printed specimens (right).	22
Figure 21. Close up of RE-α_1 loaded on the face (left) and RE-α_2 loaded on the edge (right).....	22
Figure 22. RA_R_2.30t_w (left), RA_L_2.30t_w (middle), RA_M_2.30t_w (right). Shapes are to scale within the figure.	23
Figure 23. Top row: RE-α_R_1.38t_w (left), RE-α_L_1.38t_w (middle), RE-α_M_1.38t_w (right). Middle row: RE-β_R_1.38t_w (left), RE-β_L_1.38t_w (middle), RE-β_M_1.38t_w (right). Bottom row: RE-γ_R_1.38t_w (left), RE-γ_L_1.38t_w (middle), RE-γ_M_1.38t_w (right). Shapes are to scale within the figure.	23
Figure 24. Effect of Cell Wall thickness of RA on the honeycomb elastic modulus under compression in the 1-direction (top) and 2-direction (bottom).	26
Figure 25. Top: Parametric boundary thickness analysis of RE-α in the 1-direction. Middle: Array modulus vs boundary thickness of RE-α in the 1-direction. Bottom: Relative density vs boundary thickness of RE-α in the 1-direction.	28
Figure 26. Top: Parametric boundary thickness analysis of RE-α in the 2-direction. Middle: Array modulus vs boundary thickness of RE-α in the 2-direction. Bottom: Relative density vs boundary thickness of RE-α in the 2-direction.	29
Figure 27. Top: Parametric boundary thickness analysis of RE-β in the 1-direction. Middle: Array modulus vs boundary thickness of RE-β in the 1-direction. Bottom: Relative density vs boundary thickness of RE-β in the 1-direction.....	31
Figure 28. Top: Parametric boundary thickness analysis of RE-β in the 2-direction. Middle: Array modulus vs boundary thickness of RE-β in the 2-direction. Bottom: Relative density vs boundary thickness of RE-β in the 2-direction.....	32
Figure 29. Top: Parametric boundary thickness analysis of RE-γ in the 1-direction. Middle: Array modulus vs boundary thickness of RE-γ in the 1-direction. Bottom: Relative density vs boundary thickness of RE-γ in the 1-direction.....	34

Figure 30. Top: Parametric boundary thickness analysis of RE-γ in the 2-direction. Middle: Array modulus vs boundary thickness of RE-γ in the 2-direction. Bottom: Relative density vs boundary thickness of RE-γ in the 2-direction.....	35
Figure 31. Comparison between FEA analysis and mechanical testing of RA_R specimen.....	40
Figure 32. Mechanical test data of PLA array and representative elements in 1-direction (left) and 2-direction (right).....	41
Figure 33. Mechanical test data of PETG array and representative elements in 1-direction (left) and 2-direction (right).....	41
Figure 34. Mechanical test data of ABS array and representative elements in 1-direction (left) and 2-direction (right).....	41
Figure 35. Boundary thickness/wall thickness ratio vs relative density of RE-α specimens.	43
Figure 36. Boundary thickness/wall thickness ratio vs relative density of RE-β specimens.	43
Figure 37. Boundary thickness/wall thickness ratio vs relative density of RE-γ specimens.	43
Figure 38. Even at extreme boundary thicknesses, few specimens did not reach the stress of the array exhibited at 5% strain. This is due to initial height of the specimen not scaling with the overall size of the specimen.	44
Figure 39. RR vs RD fitting (left) and residuals (right) of RE-α_2 specimens.....	45
Figure 40. RR vs RD fitting (left) and residuals (right) of RE-β_1. specimens.....	45
Figure 41. RR vs RD fitting (left) and residuals (right) of RE-γ_1. specimens.....	45
Figure 42. RR vs RD fitting (left) and residuals (right) of RE-γ_2. specimens.....	45
Figure 43. Applying the representative element approach to re-entrant (top row), tetra-chiral (middle row) and hybrid (bottom row) honeycombs.	47

List of Tables

Table 1. Relationship between α, E^* and E_{inf}^* in a regular hexagonal honeycomb. (Adapted from Onck, Andrews and Gibson ‘<i>Size effects in ductile cellular solids. Part I: modeling</i>’ 2001)	11
Table 2. Geometries of reference array and representative elements	15
Table 3. Stress and strain definitions for all specimens in the 1 and 2-directions..	17
Table 4. 3D printing parameters. (Parameters may vary with different printers and filament brands)	21
Table 5. Naming of virtual test specimens.....	25
Table 6. Parametric analysis of RA, RE-α, RE-β and RE-γ under compression in the 1-direction. Lower standard error percentages suggest linearity.....	38
Table 7. Parametric analysis of RA, RE-α, RE-β and RE-γ under compression in the 2-direction. Lower standard error percentages suggest linearity.....	39
Table 8. The sign of 2nd derivative of the trendline functions of array modulus vs t_b and relative density vs t_b among all representative elements. A positive 2nd derivative indicates up-increasing concavity, a negative 2nd derivative indicated down-increasing concavity and values close to 0 indicate linear behavior.....	42
Table 9. Relative density range of applicability of boundary walls among all representative elements	44
Table 10. Fitting parameters and goodness of fit data of RE-α_2, RE-β_1, RE-γ_1 and RE-γ_2	46

List of Symbols and Abbreviations

1 Symbols (In Order of Appearance)

ρ : Density

σ : Stress

ε : Strain

θ : Angle of Honeycomb's Inclined Walls

α : Size Effect Proportionality

E: Elastic Modulus

E*: Effective Modulus of Honeycomb

E*_{inf}: Effective Modulus of Infinite Honeycomb

ν : Poisson's Ratio

δ : Deflection

I: Moment of Inertia

A: Extensional Stiffness Matrix

B: Coupling Stiffness Matrix

D: Bending Stiffness Matrix

2 Abbreviations (In Order of Appearance)

FEM: Finite Element Method

FEA: Finite Element Analysis

CNC: Computerized Numerical Control

3D: 3-Dimensional

CLBT: Classical Laminated Beam Theory

D.O.F: Degrees of Freedom

PLA: Polylactic Acid

PLA+: A Commercial PLA Filament with Additives to Make It Less Brittle

PETG: Polyethylene Terephthalate Glycol

ABS: Acrylonitrile Butadiene Styrene

WT: Wall Thickness

RA: Reference Array

RE: Representative Element

t_b: Boundary Thickness

t_b*: Representative Boundary Thickness

RR: Representative Ratio

AS: Array Stress

RD: Relative Density

BC: Boundary Condition

PBC: Periodic Boundary Condition

1 Introduction

1.1 General Introduction

Cellular solids are low assemblies of cells with solid edges or faces, packed to fill a desired space efficiently. These structures can be found both in nature and manufactured synthetically.

Cellular solids are used in many applications for their thermal insulation properties, their high specific compressive strengths and moduli, their buoyancy, and their filtration/sieving capabilities. Early applications of honeycombs were mostly done to utilize their out-of-plane properties; however, some recent studies have focused on buckling and localized and progressive deformation behavior of honeycombs under in-plane compressive loads.

Out-of-plane[1]–[9] and in-plane[3], [6], [10]–[27] properties of honeycomb core structures have been studied both experimentally and theoretically. Theoretical works ranges from analytical calculations to Finite Element Method analysis (FEM) for determination of mechanical properties.

In this work, various physical analogues are studied under compression. Low-deformation compressive moduli of these structures are then correlated to the corresponding larger array.

One of the most important properties of these solids are their relative densities. Relative density can be expressed as[28]:

$$relative\ density = \frac{\rho^*}{\rho_s} \quad (Eq. 1)$$

where ρ^* is the density of the cellular material and ρ_s is the density of the solid comprising the walls of the cellular solid. Commercial cellular solids can have relative densities ranging from 0.001 to 0.5; after which cell walls are too thick to warrant the use of cellular solids. With increasing relative density, the cell walls thicken and the voids within the structure shrink.

Hexagonal honeycombs are among the simplest, but most effective arrangement of cells. This shape gathers a lot of attention as hexagonal honeycombs are found in nature where evolution lead to such arrangements to maximize packing and stacking. Synthetic

hexagonal honeycombs can also be made in several ways: they can be pressed into half-hexagon shaped strips which can then be adhered together, can be cast into moulds in a liquid state to harden later on, can be processed in top-down approaches such as CNC milling from a bulk solid, or lastly, with the advent of additive manufacturing, 3D printed in a bottom-up approach.

Figure 1 summarizes the deformation mechanism under compression. The compression mechanics of a hexagonal honeycombs initiate with bending of cell walls. If the material behaves linearly elastic under compression, then this bending region of the compression exhibits the effective elastic modulus of the honeycomb. Following this region of compression, additional loads will start to crush individual cells progressively. The first crushed cells can initiate at any point of the honeycomb but will usually cause a cascading collapse of neighboring cells perpendicular to the load. This crushing of cells will plateau the stress-strain profile until a point where a sufficient number of cells are crushed. After this point, the bulk material starts carrying the load and a sudden peak in the stress-strain profile is observed.

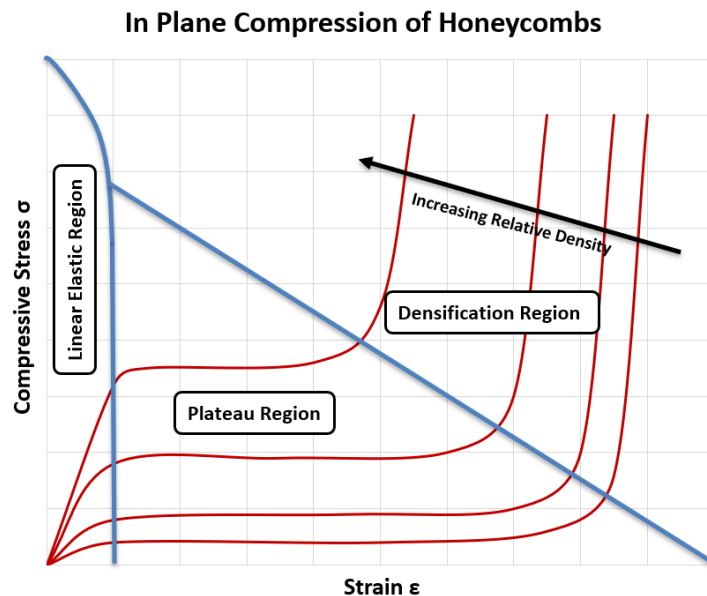


Figure 1. Behavior of honeycombs under in-plane compression (Adapted from Ashby; Gibson; 'Cellular Solids' 1997)

1.2 Analytical Models for Calculating Effective Modulus

The bending of cell walls can be described by 5 equivalent material constants: E_1^* (Young's modulus of the honeycomb in 1-direction), E_2^* (Young's modulus of the honeycomb in 2-direction), G_{12}^* (shear modulus of the honeycomb in 1-2 direction), ν_{12}^* , ν_{21}^* (Poisson's ratios of the honeycomb in 1-2 and 2-1 directions respectively). The five properties are not independent, and the following reciprocity relation holds:

$$E_1^* \nu_{21}^* = E_2^* \nu_{12}^* \quad (\text{Eq. 2})$$

In the linear region, deformation occurs mostly by the bending of inclined walls[16], [19], [29]–[31], and walls parallel to the load exhibit negligible deformation. Thus, E_1^* and E_2^* can be approximated by the bending of walls non-parallel to the load.

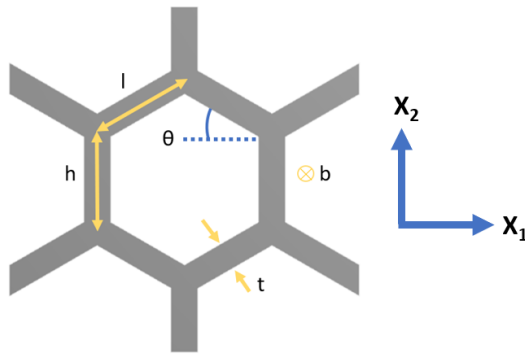


Figure 2. Dimensions and orientations in a regular hexagonal unit cell.

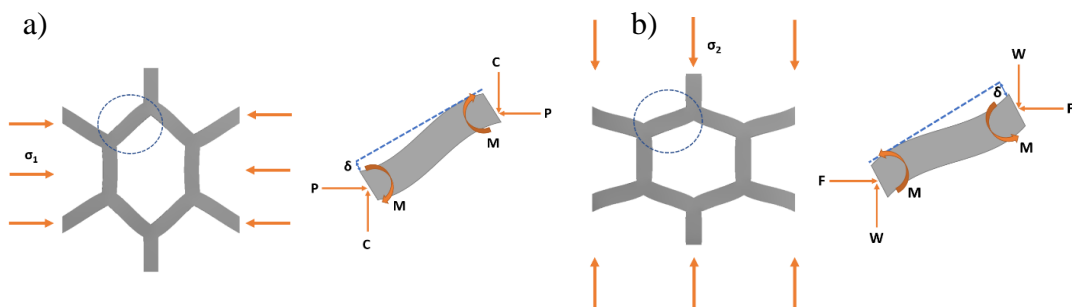


Figure 3. Forces and moments acting on inclined members under compression in the 1-direction (a) and 2-direction (b).

For direction 1, the moment bending the cell walls can be expressed as:

$$M = \frac{Pl\sin\theta}{2} \quad (\text{Eq. 3})$$

The force P causing the bending moment can be expressed as:

$$P = \sigma_1(h + l\sin\theta)b \quad (\text{Eq. 4})$$

From Roark and Youngs standard beam theory (1976), the total deflection δ of the beam can be expressed as:

$$\delta = \frac{Pl^3\sin\theta}{12E_s I} \quad (\text{Eq. 5})$$

where I, the second moment of inertia is:

$$I = \frac{bt^3}{12} \quad (\text{Eq. 6})$$

Then the strain in the 1 direction, ε_1 , becomes:

$$\varepsilon_1 = \frac{\delta\sin\theta}{l\cos\theta} \quad (\text{Eq. 7})$$

Plugging in equations 4, 5 and 6 into equation 7 yields:

$$\varepsilon_1 = \frac{\sigma_1(h + l\sin\theta)bl^3\sin\theta}{12E_s \frac{bt^3}{12}} \frac{\sin\theta}{l\cos\theta} = \frac{\sigma_1(h + l\sin\theta)l^2\sin^2\theta}{E_s t^3 \cos\theta} \quad (\text{Eq. 8})$$

Since

$$E_1^* = \frac{\sigma_1}{\varepsilon_1}, \quad (\text{Eq. 9})$$

Then:

$$E_1^* = \frac{\sigma_1}{\frac{\sigma_1(h + l\sin\theta)l^2\sin^2\theta}{E_s t^3 \cos\theta}} = \frac{E_s t^3 \cos\theta}{(h/l + \sin\theta)l^3 \sin^2\theta} = \left(\frac{t}{l}\right)^3 \frac{E_s \cos\theta}{(h/l + \sin\theta)\sin^2\theta} \quad (\text{Eq. 10})$$

Similarly, for direction 2, the moment bending the cell walls can be expressed as:

$$M = \frac{Wl\cos\theta}{2} \quad (\text{Eq. 11})$$

The force W causing the moment can be expressed as:

$$W = \sigma_2 l b \cos \theta \quad (\text{Eq. 12})$$

From Roark and Youngs standard beam theory (1976), the total deflection δ of the beam can be expressed as:

$$\delta = \frac{W l^3 \cos \theta}{12 E_s I} \quad (\text{Eq. 13})$$

where I is once again, the second moment of inertia:

$$I = \frac{b t^3}{12} \quad (\text{Eq. 14})$$

Then the strain in the 2 direction, ε_2 , becomes:

$$\varepsilon_2 = \frac{\delta \cos \theta}{h + l \sin \theta} \quad (\text{Eq. 15})$$

Plugging in equations 12, 13 and 14 into equation 15 yields:

$$\varepsilon_2 = \frac{\sigma_2 l b \cos \theta l^3 \cos \theta}{12 E_s \frac{b t^3}{12}} \frac{\cos \theta}{h + l \sin \theta} = \frac{\sigma_2 l^4 \cos^3 \theta}{E_s t^3 (h + l \sin \theta)} = \frac{\sigma_2 l^3 \cos^3 \theta}{E_s t^3 (h/l + \sin \theta)} \quad (\text{Eq. 16})$$

Since

$$E_2^* = \frac{\sigma_2}{\varepsilon_2} \quad (\text{Eq. 17})$$

Then:

$$E_2^* = \frac{\sigma_2}{\frac{\sigma_2 l^3 \cos^3 \theta}{E_s t^3 (h/l + \sin \theta)}} = \left(\frac{t}{l}\right)^3 \frac{E_s (h/l + \sin \theta)}{\cos^3 \theta} \quad (\text{Eq. 18})$$

For regular hexagonal arrays in which $\theta = 30^\circ$, we see isotropic behaviour:

$$\frac{E_1^*}{E_s} = \frac{E_2^*}{E_s} = 2.3 \left(\frac{t}{l}\right)^3 \quad (\text{Eq. 19})$$

For large deformations, the effects of axial and shear loads on the non-parallel wall deflections become non-negligible. For high deformations, stress-strain profile becomes nonlinear. The bending deflections are magnified:

$$\delta_{large} = \delta_{small} \frac{1}{1 - \frac{P_{axial}}{P_{critical}}} \quad (\text{Eq. 20})$$

where $P_{critical}$ is the Euler load. For this reason, linear studies and models only govern honeycombs in low-strain regimes.

The Poisson's ratios of hexagonal arrays can be expressed as:

$$\nu_{12}^* = -\frac{\varepsilon_2}{\varepsilon_1} = \frac{\cos^2\theta}{(h/l + \sin\theta)\sin\theta} \quad (\text{Eq. 21})$$

and

$$\nu_{21}^* = -\frac{\varepsilon_1}{\varepsilon_2} = \frac{(h/l + \sin\theta)\sin\theta}{\cos^2\theta} \quad (\text{Eq. 22})$$

For regular hexagonal arrays in which $\theta = 30^\circ$, we see that $\nu_{12}^* = \nu_{21}^* = 1$. For honeycombs in which $\theta < 0^\circ$, a negative Poisson's ratio is observed.

The relative density can also be defined by a simple geometric relation:

$$\frac{\rho^*}{\rho_s} = \frac{t/l(h/l + 2)}{2\cos\theta(h/l + \sin\theta)} \quad (\text{Eq. 23})$$

which reduces to

$$\frac{\rho^*}{\rho_s} = \frac{2}{\sqrt{3}} \frac{t}{l} \quad (\text{Eq. 24})$$

for regular honeycombs.

1.3 Refining the Analytical Model

This analytical model can be improved upon by expressing the deflections of the inclined members as the sum of deflections due to axial, shear and bending deformations[32]:

$$\delta_1 = \delta_a \cos\theta + \delta_s \sin\theta + \delta_b \sin\theta \quad (\text{Eq. 25})$$

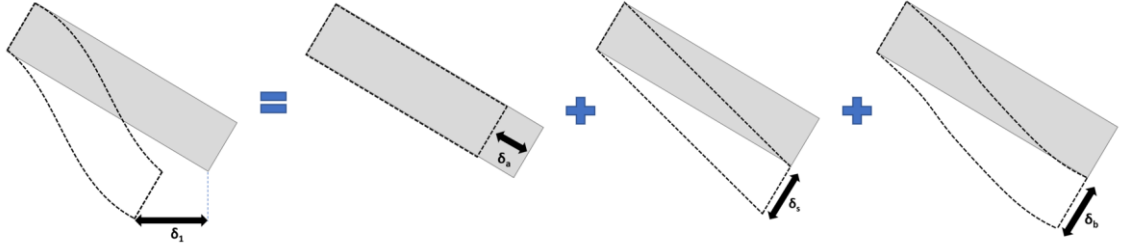


Figure 4. Deflection of inclined member represented as the sum of deflections from axial, shear and bending loads.

The axial deflection can simply be expressed from Hooke's Law:

$$\delta_a = \frac{F_1 l_b \cos\theta}{E_s b t} \quad (\text{Eq. 26})$$

The shear deflection can be expressed by Timoshenko beam theory (1970):

$$\delta_s = \frac{F_1 l_b^3 \sin\theta}{12 E_s I} (2.4 + 1.5 \nu_s \left(\frac{t}{l_b}\right)^2) \quad (\text{Eq. 27})$$

The bending deflection can be expressed by Roark and Youngs standard beam theory (1976):

$$\delta_b = \frac{F_1 l_b^3 \sin\theta}{12 E_s I} \quad (\text{Eq. 29})$$

Plugging equations 26, 27 and 28 into equation 25:

$$\delta_1 = \frac{F_1 l_b \cos\theta}{E_s b t} \cos\theta + \frac{F_1 l_b^3 \sin\theta}{12 E_s I} (2.4 + 1.5 \nu_s \left(\frac{t}{l_b}\right)^2) \sin\theta + \frac{F_1 l_b^3 \sin\theta}{12 E_s I} \sin\theta \quad (\text{Eq. 28})$$

Using the relations:

$$\varepsilon_1 = \frac{\delta_1}{l \cos\theta}, \quad (\text{Eq. 30})$$

$$\sigma_1 = \frac{F_1}{b(h + l \sin\theta)} \quad (\text{Eq. 31})$$

$$E_1^* = \frac{\sigma_1}{\varepsilon_1} \quad (\text{Eq. 9})$$

The modulus in the 1-direction then becomes:

$$E_1^* = E_s \left(\frac{t}{l_b} \right)^3 \frac{\cos\theta}{(h/l + \sin\theta)\sin^2\theta} A$$

where:

$$A = \frac{1}{1 + (2.4 + 1.5\nu_s + \cot^2\theta) \left(\frac{t}{l_b} \right)^2} \quad (\text{Eq. 33})$$

Similarly, the modulus in the 2-direction becomes:

$$E_2^* = E_s \left(\frac{t}{l_b} \right)^3 \frac{(h/l + \sin\theta)}{\cos^3\theta} B \quad (\text{Eq. 34})$$

Where

$$B = \frac{1}{1 + (2.4 + 1.5\nu_s + \tan^2\theta + \frac{2(h_b/l_b)}{\cos^2\theta}) \left(\frac{t}{l_b} \right)^2} \quad (\text{Eq. 35})$$

1.4 Limitations of Analytical and Experimental Models

1.4.1 Geometric Changes in Stiffness

Analytical models neglect the change of stiffness due to geometrical changes. When the walls of the hexagonal array are under stress, their shapes change, resulting in a change in their effective stiffness. This instantaneous change in shape affects how the geometry will respond to additional incremental load.

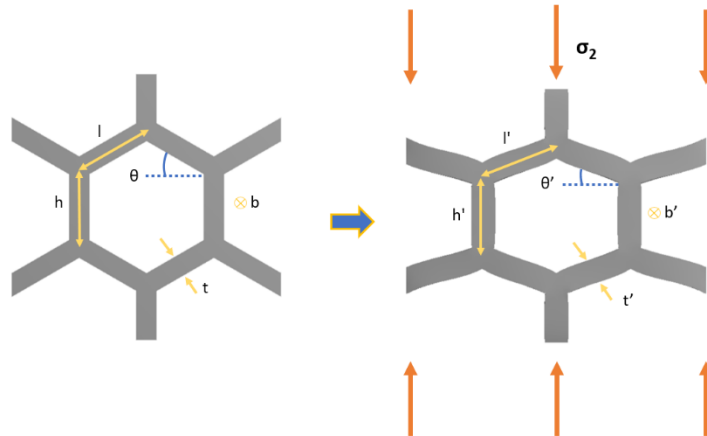


Figure 5. Change in dimensions and orientations of load-carrying members causing a change in effective stiffness.

Numerical analysis like finite element method can capture these small changes. In ANSYS® Academic Research Mechanical, Release 19.2, this effect can be accounted for with the ‘Large Deflection’ option.

1.4.2 Isotropic Assumption

Classical analytical models were theorized for isotropic materials. There have been efforts to modify them for laminated multi-material walls[5]. Honeycombs made from an assorted layup of fiber reinforced composites are also of increasing interest which can greatly complicate the stiffness response of the honeycomb. In the case of orthotropic materials like continuous fiber reinforced polymer matrix composites, Wang and Wang (2018) theorized that Ashby and Gibson’s analytical honeycomb stiffness model can be adapted by modifying the moments and the longitudinal forces to behave in accordance to composite’s A (extensional-stiffness), B (coupling-stiffness) and D (bending stiffness) matrices from Classical Laminated Beam Theory (CLBT).

With these modifications in mind, for an orthotropic honeycomb, the moments and longitudinal force becomes:

$$M = B\varepsilon_x + D \frac{d^2w}{dx^2} \quad (\text{Eq. 36})$$

$$N = A\varepsilon_x + B \frac{d^2w}{dx^2} \quad (\text{Eq. 37})$$

where:

$$A = \sum_{i=1}^n E_{si}(z_i - z_{i-1}) \quad (\text{Eq. 38})$$

$$B = \frac{1}{2} \sum_{i=1}^n E_{si}(z_i^2 - z_{i-1}^2) \quad (\text{Eq. 39})$$

$$D = \frac{1}{3} \sum_{i=1}^n E_{si}(z_i^3 - z_{i-1}^3) \quad (\text{Eq. 40})$$

where E_{si} is the elastic modulus of i th ply, and z_i is the distance between the bottom surface of the bottom ply to top surface of the i th ply.

If no normal cell wall stress is assumed, we are left with the bending moment that works to bend the inclined cell walls of the honeycomb:

$$M = \left(D - \frac{B^2}{A}\right) \frac{d^2y}{dx^2} \quad (\text{Eq. 43})$$

where x is the longitudinal and y is the transverse direction of the laminate comprising the cell walls. Since $(D - B^2/A)$ is the effective flexural rigidity, the effective modulus of the honeycomb becomes:

$$E_1^* = E_s \left(\frac{t}{l_b}\right)^3 \frac{\cos\theta}{(h/l + \sin\theta)\sin^2\theta} \left(D - \frac{B^2}{A}\right) \quad (\text{Eq. 41})$$

$$E_2^* = E_s \left(\frac{t}{l_b}\right)^3 \frac{(h/l + \sin\theta)}{\cos^3\theta} \left(D - \frac{B^2}{A}\right) \quad (\text{Eq. 42})$$

1.4.3 Size Effect

Furthermore, cellular solids are, in practice, finite objects, and the boundary conditions imposed upon them in real life differ from numerical studies with periodic boundary conditions. Several works have been done on the ‘size effect’ on the response of honeycombs[33]–[36].

The same honeycomb will react to in-plane compression differently depending on how many cells are found in the particular structure, even after normalization by area. Generally, an increasing (axial # of cells / transverse # of cells) ratio will result in an increase in effective modulus[37].

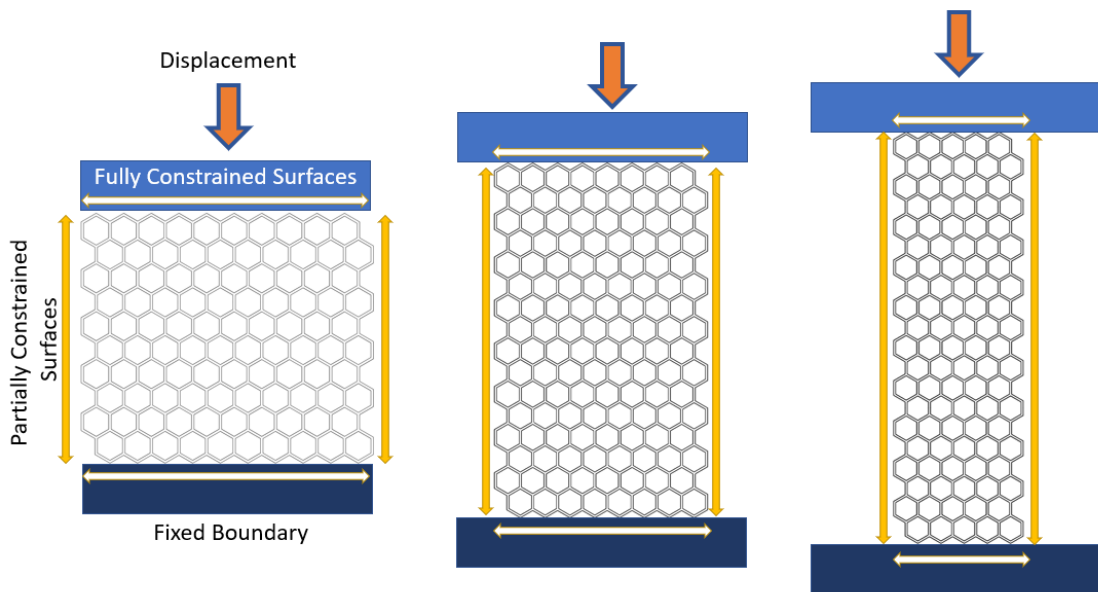


Figure 6. Different shapes of honeycombs with equally dimensioned unit cells. Different boundary conditions result in different moduli.

Onck, Andrews and Gibson (2001) determined that there exists a relation between α (the width of the honeycomb divided by width of a single cell $D = \sqrt{3}L$, refer to Figure 7), E^* (effective modulus of the honeycomb) and E_{inf}^* (effective modulus of the same honeycomb extending in 1 and 2-directions to infinity):

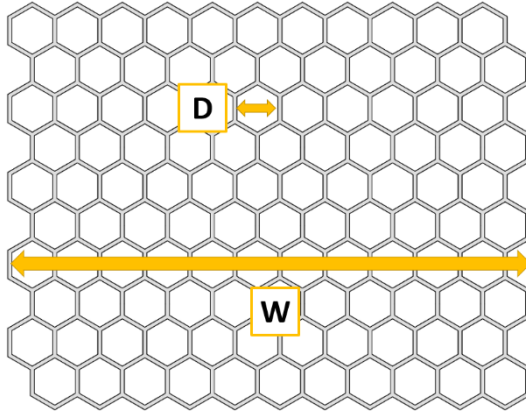


Figure 7. W and D lengths in size parameter ' α '.

$\alpha = \frac{W}{D}$	$\frac{E^*}{E_{inf}^*}$
$1 \leq \alpha < 2$	$\frac{1}{2\alpha}$
$2 \leq \alpha < 3$	$\frac{41}{28\alpha}$
$3 \leq \alpha < 4$	$\frac{165}{67\alpha}$
$8 \leq \alpha < 9$	$\frac{7.45}{\alpha}$
$16 \leq \alpha < 17$	$\frac{15.45}{\alpha}$

Table 1. Relationship between α , E^* and E_{inf}^* in a regular hexagonal honeycomb. (Adapted from Onck, Andrews and Gibson 'Size effects in ductile cellular solids. Part I: modeling' 2001)

1.5 Research Hypothesis

Contrary to numerical analysis, it is significantly challenging, if not impossible to apply periodic boundary conditions to an experimental setting. To realize or simulate these boundary conditions practically, a unit cell can be designed to be a representation of a reference array. This unit cell by design, when tested experimentally, should exhibit the behavior of the reference array despite its much-reduced size and preparation cost.

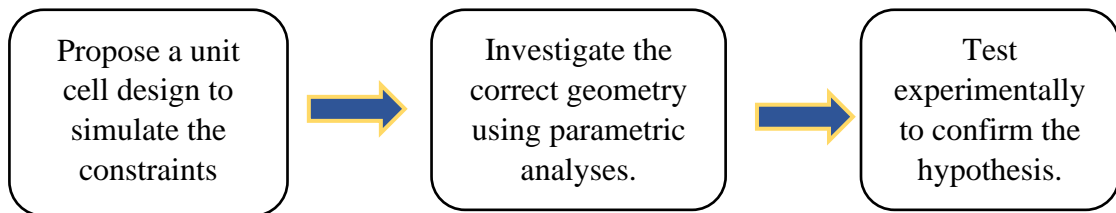


Figure 8. Flowchart summarizing research steps.

2 Methods

2.1 Representative Element and Reference Array Design

Computational representative volume elements (RVE) have been investigated in thoroughly for in-plane behavior of honeycombs[32], [38], [39]. Some of these representative volume elements are shown in Figure 9.

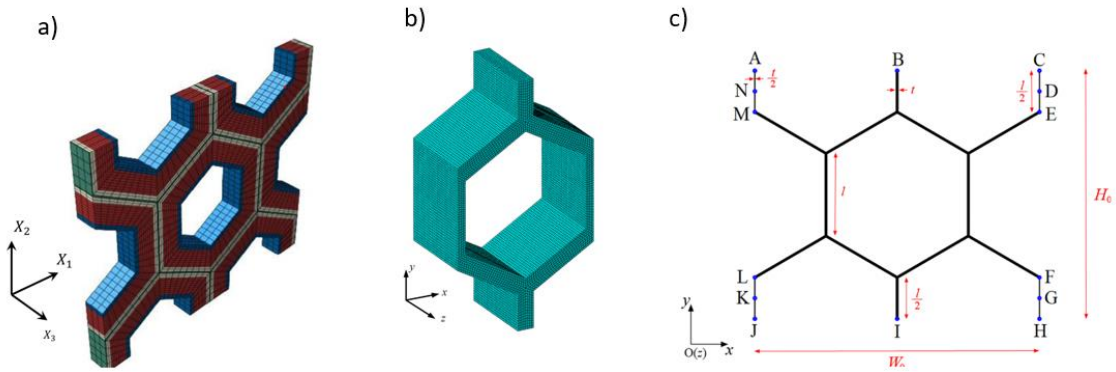


Figure 9. RVE's under periodic boundary conditions from various research*.

These RVE's are sections taken from the whole structure and they can be stacked periodically to create the infinite array.

To design a representative test element that would practically simulate an array of many cells, constraints must be implied so that a repeating unit cell within the array would react similarly to deformation.

If a single unit cell (for hexagonal honeycombs, a single hexagon) is isolated and tested under compression, the non-inclined walls are free to translate in the transverse direction (Figure 10).

*: a) Malek, Sardar; Gibson, Lorna *Effective elastic properties of periodic hexagonal honeycombs*, 2015
b) Zhao, Yang; Ge, Meng; Ma, Wenlai *The effective in-plane elastic properties of hexagonal honeycombs with consideration for geometric nonlinearity*, 2020
c) Chen, Yu; Hu, Hong *In-plane elasticity of regular hexagonal honeycombs with three different joints: A comparative study*, 2020

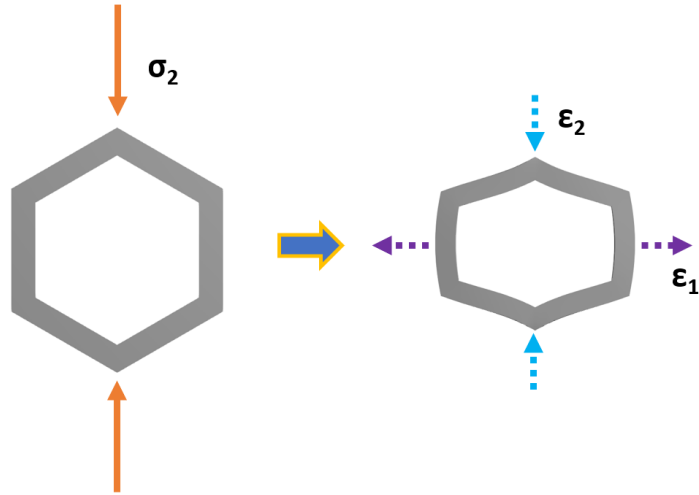


Figure 10. Deformation of an isolated unit cell under compression.

However, within an array under a distributed load, the transverse translation of non-inclined walls of a unit cell in the center of the array is constrained by the neighboring unit cells (Figure 11) as the whole assembly should work in concert. This causes the non-inclined walls to act as rigid bodies that anchor the bending inclined walls. Note that moving away from the central cell to the sides, the number of neighboring cells in each of the sides of the cell starts to differ. And getting closer to the array's edge, this disparity of prohibitive structures causes the cells to undergo transverse deformation. Thus, the overall array structure will exhibit transverse deformation (Figure 12).

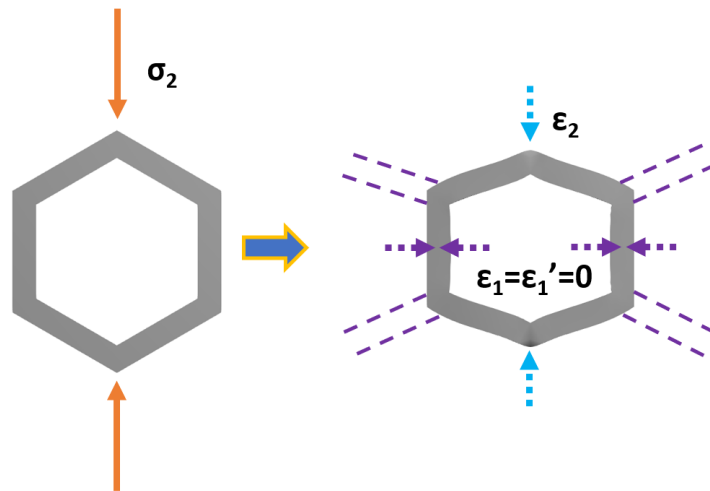


Figure 11. Deformation of a central cell within the array.

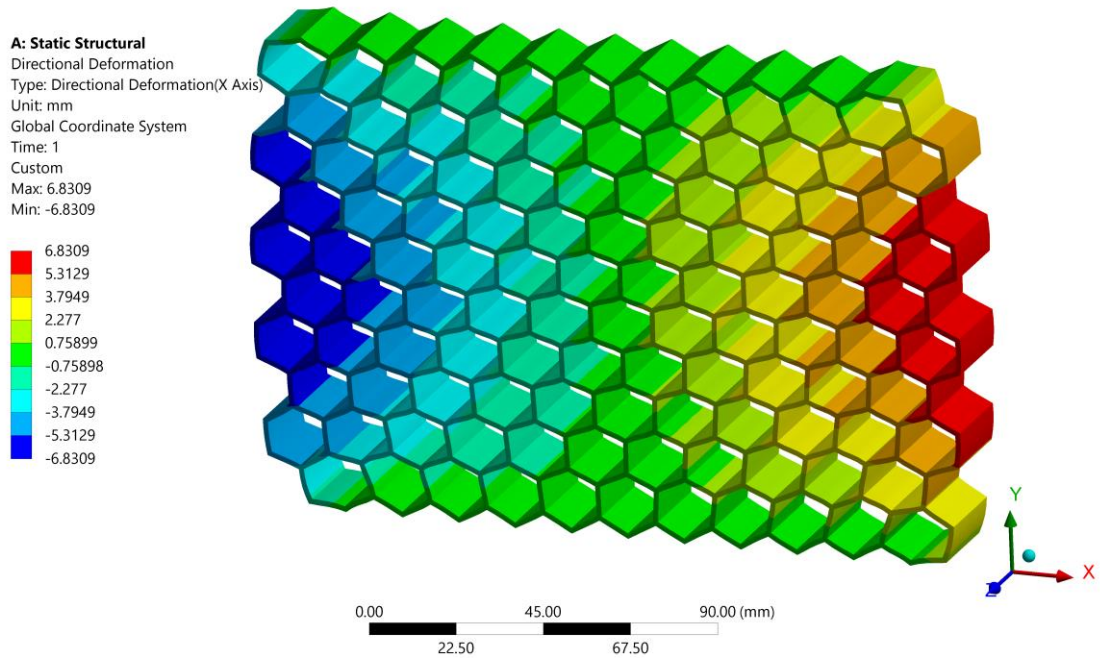


Figure 12. Transverse directional deformation of an array under compression in the 2-direction (y-axis in the image). Note that the central array experiences no transverse deformation and the edges show maximum transverse deformation (red and dark blue)

When designing a representative testing cell, this constrained deformation of non-inclined walls must be considered. A single basic repeating unit cell tested experimentally does not simulate the larger array accurately. Instead, the basic repeating unit cell was extended to include the complete joint structure and segments of its closest neighboring unit cells. When this so called ‘spider-web’ structure (Figure 13) is enclosed by a shell, the prohibitive effect of the original neighboring cells can be simulated. To generalize the approach for enclosing these shells, 3 models are proposed that could arguably be applicable to any periodic 2D cellular structure (Table 2). The dimensions for strain calculation and stress normalization were based on the deformation of the spider-web structure (Figure 14).

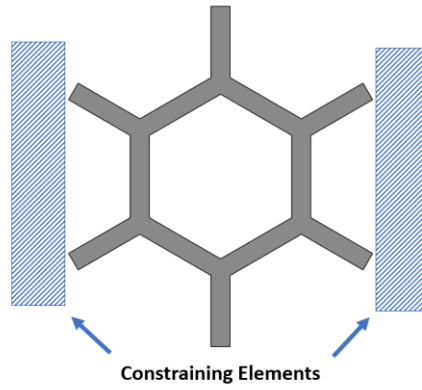


Figure 13. The spider-web structure and the constraints imposed on these structures by an enclosed shell.

Designation	Description	Visualization
10x10 Reference Array (RA)	A larger array with 10 cells in the 1-direction and 10 cells in the 2-direction	
Representative Element 1 (RE- α)	A RE enclosed by a parametric shell, with vertexes on closest joints	
Representative Element 2 (RE- β)	A RE enclosed by a parametric shell, with vertexes on closest neighboring cell centers	
Representative Element 3 (RE- γ)	A RE surrounded by closest neighboring cells, enclosed by parametric shell	

Table 2. Geometries of reference array and representative elements

Note that these representative elements are no longer typical unit cells. They cannot be added together with a periodicity to form the targeted larger array. Representative elements are separate, but equivalent structures to the larger array for investigation of in-plane elastic properties.

A specific thickness of this enclosing boundary is expected to exhibit the compressive response of the larger array. This thickness varies with the wall thickness, the wall length, and the inclined wall angle of the simulated array. **Thus, this boundary thickness ‘ t_b ’ behaves akin to the material constants of a bulk material.**

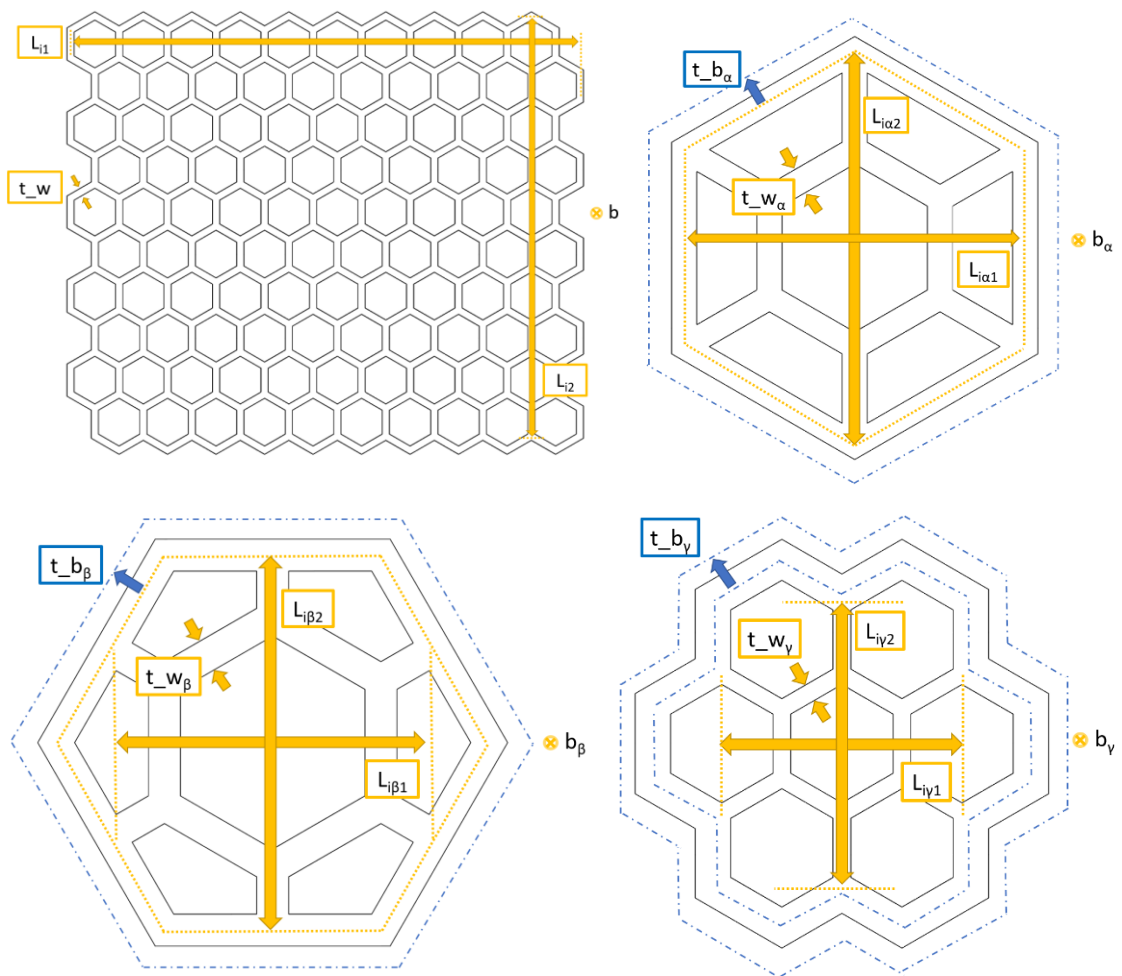


Figure 14. Dimensions of RA (top-left), RE- α (top-right), RE- β (bottom-left) and RE- γ (bottom-right) for FEM and experimental analysis.

The dimensions for strain, stress and relative density calculation for each specimen are:

Specimen	Stress (1-direction)	Strain (1-direction)	Stress (2-direction)	Strain (2-direction)
RA	$\frac{F}{(L_{i2}) b}$	$\frac{\Delta L_{i1}}{L_{i1}}$	$\frac{F}{(L_{i1}) b}$	$\frac{\Delta L_{i2}}{L_{i2}}$
RE- α	$\frac{F}{(L_{i\alpha2}) b_{\alpha}}$	$\frac{\Delta L_{i\alpha1}}{L_{i\alpha1}}$	$\frac{F}{(L_{i\alpha1}) b_{\alpha}}$	$\frac{\Delta L_{i\alpha2}}{L_{i\alpha2}}$
RE- β	$\frac{F}{(L_{i\beta2}) b_{\beta}}$	$\frac{\Delta L_{i\beta1}}{L_{i\beta1}}$	$\frac{F}{(L_{i\beta1}) b_{\beta}}$	$\frac{\Delta L_{i\beta2}}{L_{i\beta2}}$
RE- γ	$\frac{F}{(L_{i\gamma2}) b_{\gamma}}$	$\frac{\Delta L_{i\gamma1}}{L_{i\gamma1}}$	$\frac{F}{(L_{i\gamma1}) b_{\gamma}}$	$\frac{\Delta L_{i\gamma2}}{L_{i\gamma2}}$

Table 3. Stress and strain definitions for all specimens in the 1 and 2-

Where F is the force reaction due to displacement boundary condition.

2.2 Finite Element Analysis

ANSYS® Workbench 19.2 Static Structural Module was used to conduct the FEA Simulations. A linear elastic model was selected to represent the PLA specimen. To determine elastic modulus and Poisson's ratio, dog bone specimens were printed and tested in tension with a UTM. Print orientation of the dog bone sample was kept the same as honeycomb and unit cell specimens to account for the same anisotropy inherent in 3D printing. Longitudinal and transverse 350 Ohm Omega strain gauges were used in unison to measure the Poisson's ratio. Values of $E=2780$ MPa and $\nu=0.25$ were in agreement with the literature[40] [41].

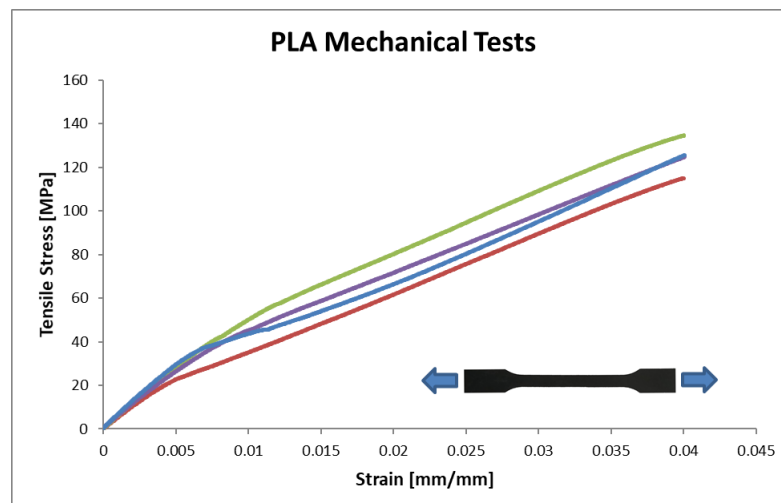


Figure 15. Mechanical tests of PLA for modulus determination.

Large deflection was enabled to simulate geometric effects on elasticity. Weak springs with forces in the order of 0.001% or less of the reaction forces were used to eliminate mechanical instability. Meshes around the joints were refined edgewise to capture joint-related deflections more accurately. Boundary conditions fixed the geometry with 0 D.O.F. on the bottom edge/edges for RA, RE- α , RE- γ and on the bottom face for RE- β . A constant displacement was applied from the top edge/edges of RA, RE- α , RE- γ and on the top face for RE- β . D.O.F. were restrained in the other two axes. These boundary conditions were selected to simulate the testing conditions in a compression test.

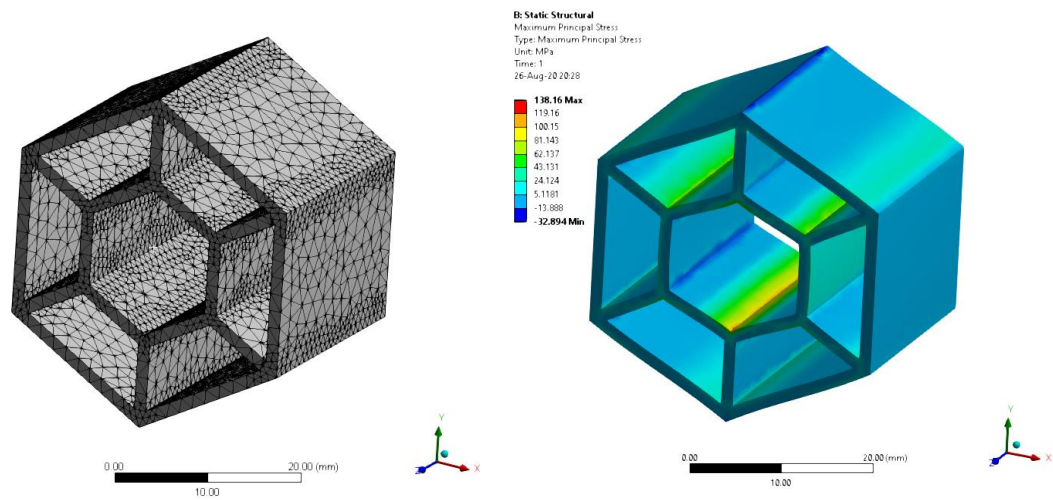


Figure 16. Typical mesh applied to specimens (left) and a specimen under deformation showing maximum principal stress (right).

Analysis Type	Geometry Type	Solver Type	Weak Springs	Large Deflection	Inertial Relief	Material Model
Static Structural	3D	Direct	On	On	Off	Linear Elastic/ Isotropic
# of Steps	Load BC	Constraint BC	Load BC	Constraint BC	Input Parameters	Output Parameter
1	Displacement $u(y)$, $u(x)=u(z)=0$	Fixed Support	Displacement $u(y)$, $u(x)=u(z)=0$	Fixed Support	t_w, t_b	Force Reaction (y) @ Supports
Element Size	Element Type	Element Order	# of Elements Along Walls	Mesh Refinement	Meshing Method	Meshing Algorithm
2 mm	SOLID186	Quadratic	>10	3, Around Joint Edges	Tetrahedrons	Patch Conforming

Table 4. ANSYS® Workbench simulation parameters.

The following procedure was followed for the parametric analysis of all specimens:

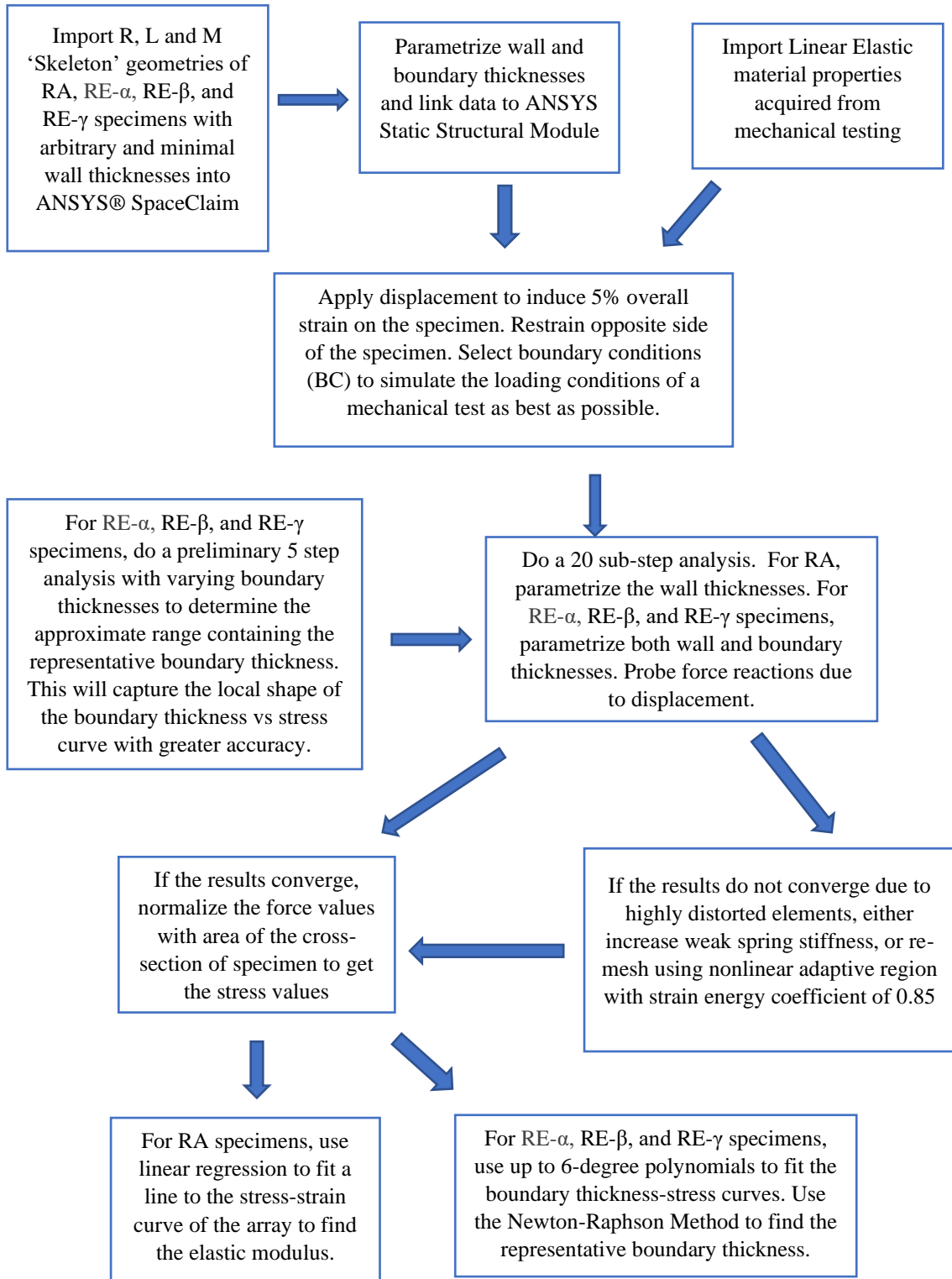


Figure 17. Flowchart for FEM analysis

2.3 Design and 3D Printing of Specimens

Arrays and representative elements were modeled in SOLIDWORKS® using parametric dimensions for wall thickness, boundary thickness, and wall length. A sufficiently high depth of 24mm was selected among all specimens to ensure no buckling occurs during compression testing. Models were exported in ‘.stl’ format to be sliced in PrusaSlicer® 2.0 software.

Specimens were sliced with their out-of-plane orientation coinciding with the printer’s z-axis. This was done to eliminate the need for supports during printing and keep material properties constant in the in-plane axes.

Physical analogues were manufactured using a Prusa® MK3S FDM printer in batches. All specimens were printed with Esun® PLA+ filament (silver color). Several printing parameters were tested to optimize layer adhesion, gap fill, stringing, bed adhesion, hot end wobble and other printing artifacts. An enclosure was used to keep the chamber temperature slightly higher than room temperature.

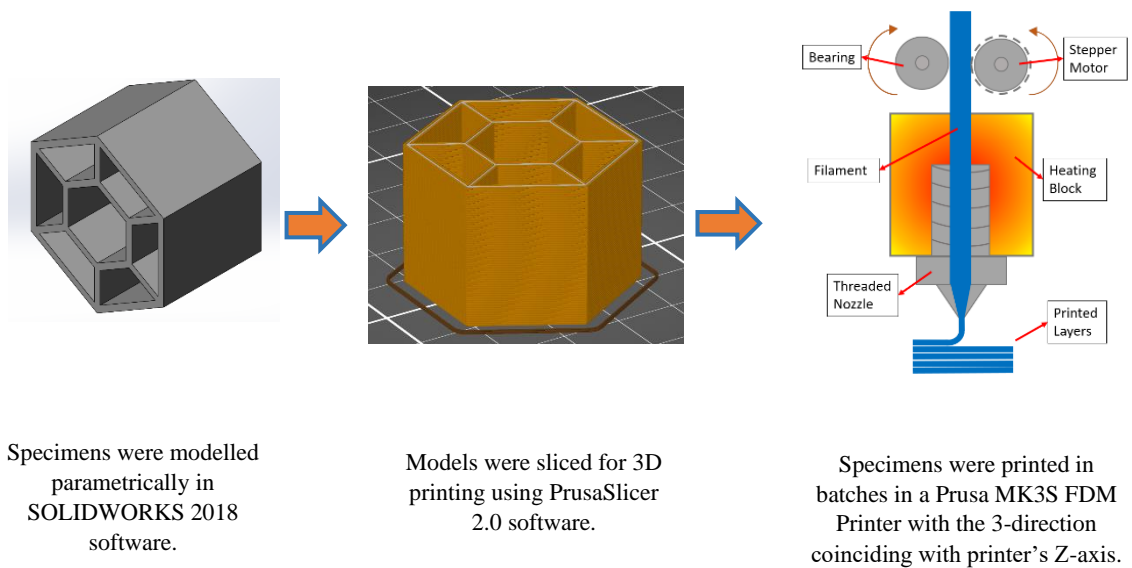


Figure 18. Flowchart for FDM manufacturing.

Printing parameters:

Layer Height	Nozzle Temperature	Print Bed Temperature	Max Print Speed	Nozzle Diameter	Perimeter Width	Infill Percentage
0.2 mm	210° (PLA+) 245° (PETG) 250° (ABS+)	60° (PLA+) 90° (PETG) 100° (ABS+)	80 mm/s	0.4 mm	0.46 mm	100%
Extrusion Multiplier	Number of Perimeters	Infill Angle	# of Top/Bottom Layers	Seam Alignment	Infill/Perimeter Overlap	Retraction Compensation
0.94	1	40°	5/4	Random	25%	0.03 mm

Table 5. 3D printing parameters. (Parameters may vary with different printers and filament brands)

2.4 Mechanical testing

Uniaxial compression tests (up to %5 contraction) were performed with a Zwick/Roell Z100 Universal Testing Machine. A strain rate of 5 mm/min was utilized. Thin aluminum tape was adhered to both compression plates and were allowed to be indented during the test. This negligible deformation in the larger scope of things prevented slippage when applying edge loads as shown. The rotating ball joint of the mobile compression plate were also fixed perpendicularly to the load direction to reduce the D.O.F. The force readings were done through a 100kN load cell. Displacement readings were done from the crosshead movement.

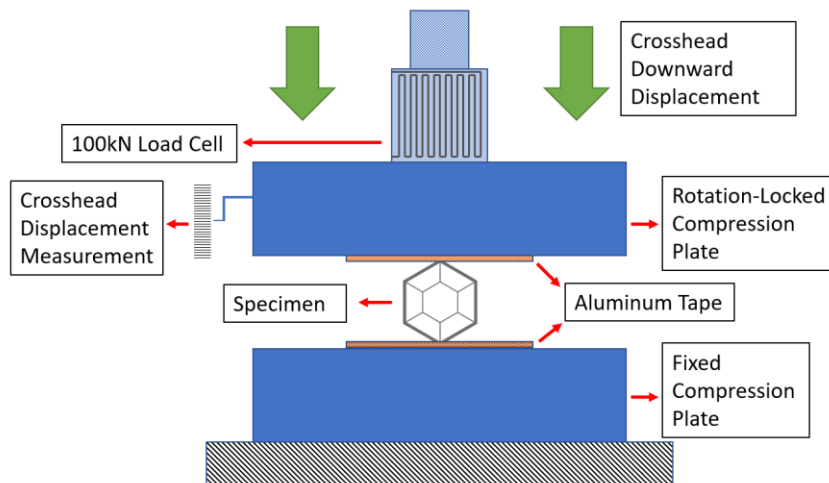


Figure 19. Schematic of the compression jig.

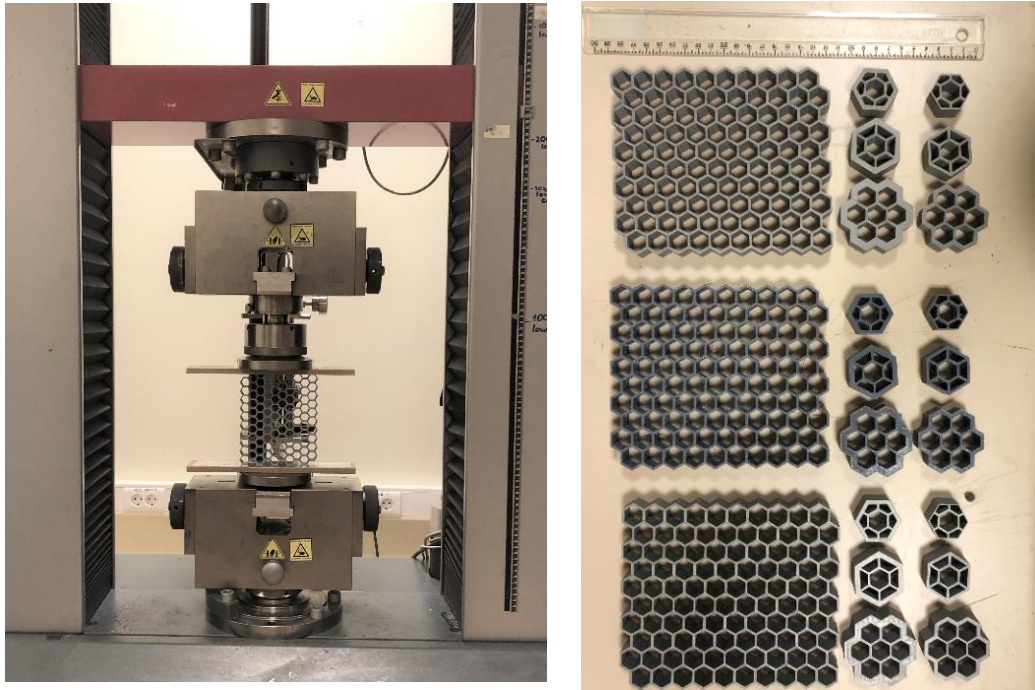


Figure 20. Testing setup (left), 3D printed specimens (right).

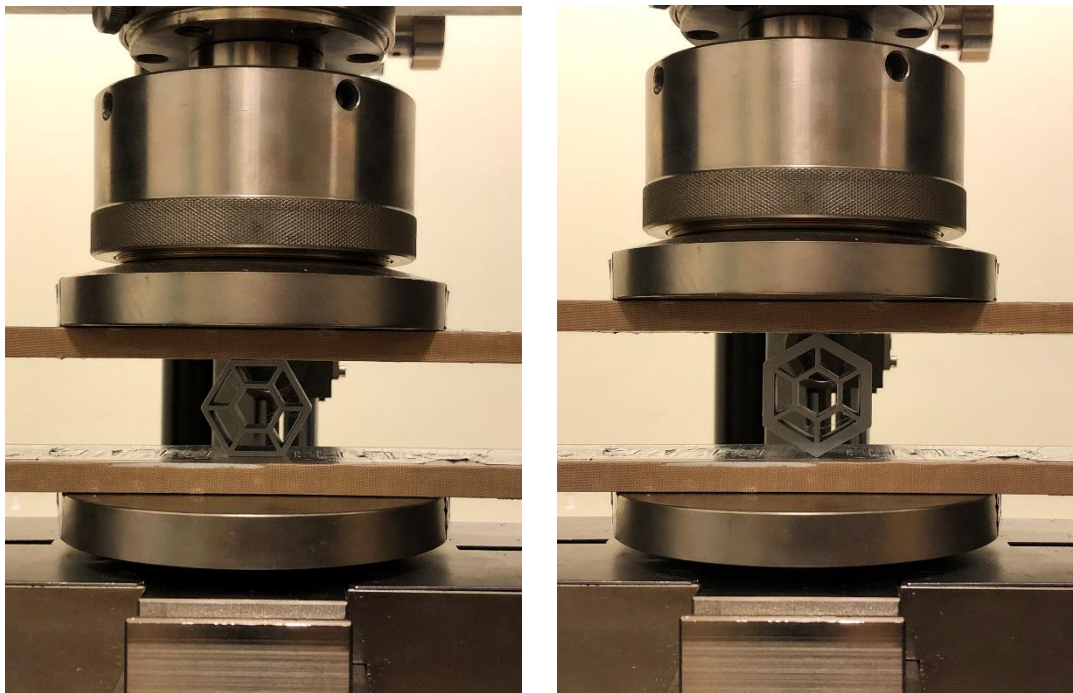


Figure 21. Close up of RE- α _1 loaded on the face (left) and RE- α _2 loaded on the edge (right).

3 Results & Discussion

3.1 FEA Results

3.1.1 Naming Convention

Specimens are grouped as 4 different geometries: **RA** (reference array), **RE- α** (representative element alpha), **RE- β** (representative element beta) and **RE- γ** (representative element gamma). These geometries have 3 subgroups: **R** (for ‘regular’), **L** (for ‘larger’) and **M** (for ‘mixed’: a mix of long and short cell walls). Throughout this work, R, L and M specimens have been color coded: **R in red**, **L in cyan**, and **M in green**. Each of these subgroups have 5 different wall thickness specimens, denoted with **_0.46t_w**, **_0.92t_w**, **_1.38t_w**, **_1.84t_w** and **_2.30t_w**. Refer to Figure 22 and Figure 23 for visualization of several example specimens. All specimens are investigated in both **_1** and **_2** directions.

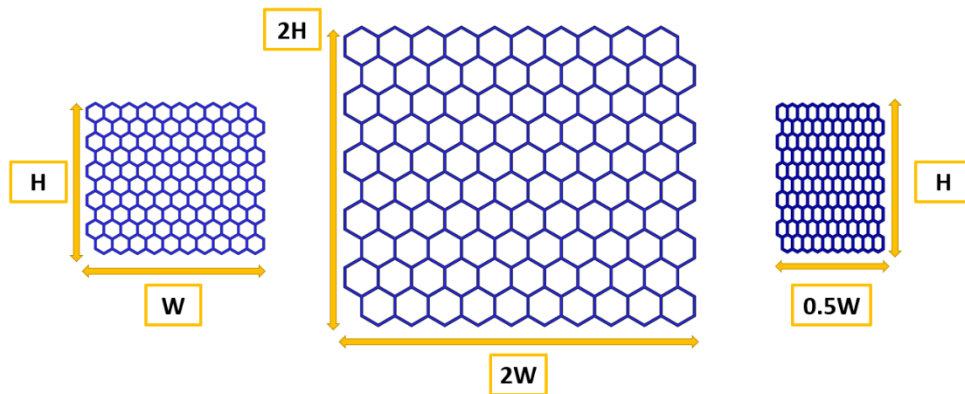


Figure 22. RA_R_2.30t_w (left), RA_L_2.30t_w (middle), RA_M_2.30t_w (right). Shapes are to scale within the figure.

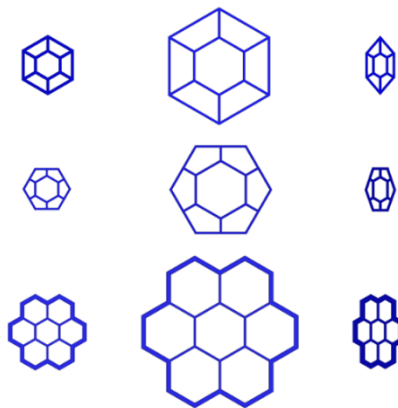


Figure 23. Top row: RE- α _R_1.38t_w (left), RE- α _L_1.38t_w (middle), RE- α _M_1.38t_w (right). Middle row: RE- β _R_1.38t_w (left), RE- β _L_1.38t_w (middle), RE- β _M_1.38t_w (right). Bottom row: RE- γ _R_1.38t_w (left), RE- γ _L_1.38t_w (middle), RE- γ _M_1.38t_w (right). Shapes are to scale within the figure.

3.1.2 List of Virtual Test Specimens

Designation	Wall Thickness (mm)	l (mm)	h (mm)	θ (°)	E_s (MPa)	ν_s	Relative Density	# of Cells	Parametric Boundary (Yes/No)
RA_R_0.46t_w	0.46	9	9	30	2780	0.25	0.059	100	No
RA_R_0.92t_w	0.92	9	9	30	2780	0.25	0.118	100	No
RA_R_1.38t_w	1.38	9	9	30	2780	0.25	0.177	100	No
RA_R_1.84t_w	1.84	9	9	30	2780	0.25	0.236	100	No
RA_R_2.30t_w	2.30	9	9	30	2780	0.25	0.295	100	No
RA_L_0.46t_w	0.46	18	18	30	2780	0.25	0.030	100	No
RA_L_0.92t_w	0.92	18	18	30	2780	0.25	0.059	100	No
RA_L_1.38t_w	1.38	18	18	30	2780	0.25	0.089	100	No
RA_L_1.84t_w	1.84	18	18	30	2780	0.25	0.118	100	No
RA_L_2.30t_w	2.30	18	18	30	2780	0.25	0.148	100	No
RA_M_0.46t_w	0.46	4.5	9	30	2780	0.25	0.094	100	No
RA_M_0.92t_w	0.92	4.5	9	30	2780	0.25	0.189	100	No
RA_M_1.38t_w	1.38	4.5	9	30	2780	0.25	0.283	100	No
RA_M_1.84t_w	1.84	4.5	9	30	2780	0.25	0.378	100	No
RA_M_2.30t_w	2.30	4.5	9	30	2780	0.25	0.472	100	No
RE- α _R_0.46t_w	0.46	9	9	30	2780	0.25	-	1	Yes
RE- α _R_0.92t_w	0.92	9	9	30	2780	0.25	-	1	Yes
RE- α _R_1.38t_w	1.38	9	9	30	2780	0.25	-	1	Yes
RE- α _R_1.84t_w	1.84	9	9	30	2780	0.25	-	1	Yes
RE- α _R_2.30t_w	2.30	9	9	30	2780	0.25	-	1	Yes
RE- α _L_0.46t_w	0.46	18	18	30	2780	0.25	-	1	Yes
RE- α _L_0.92t_w	0.92	18	18	30	2780	0.25	-	1	Yes
RE- α _L_1.38t_w	1.38	18	18	30	2780	0.25	-	1	Yes
RE- α _L_1.84t_w	1.84	18	18	30	2780	0.25	-	1	Yes
RE- α _L_2.30t_w	2.30	18	18	30	2780	0.25	-	1	Yes
RE- α _M_0.46t_w	0.46	4.5	9	30	2780	0.25	-	1	Yes
RE- α _M_0.92t_w	0.92	4.5	9	30	2780	0.25	-	1	Yes
RE- α _M_1.38t_w	1.38	4.5	9	30	2780	0.25	-	1	Yes
RE- α _M_1.84t_w	1.84	4.5	9	30	2780	0.25	-	1	Yes
RE- α _M_2.30t_w	2.30	4.5	9	30	2780	0.25	-	1	Yes
RE- β _R_0.46t_w	0.46	9	9	30	2780	0.25	-	1	Yes
RE- β _R_0.92t_w	0.92	9	9	30	2780	0.25	-	1	Yes
RE- β _R_1.38t_w	1.38	9	9	30	2780	0.25	-	1	Yes
RE- β _R_1.84t_w	1.84	9	9	30	2780	0.25	-	1	Yes
RE- β _R_2.30t_w	2.30	9	9	30	2780	0.25	-	1	Yes
RE- β _L_0.46t_w	0.46	18	18	30	2780	0.25	-	1	Yes
RE- β _L_0.92t_w	0.92	18	18	30	2780	0.25	-	1	Yes
RE- β _L_1.38t_w	1.38	18	18	30	2780	0.25	-	1	Yes
RE- β _L_1.84t_w	1.84	18	18	30	2780	0.25	-	1	Yes
RE- β _L_2.30t_w	2.30	18	18	30	2780	0.25	-	1	Yes
RE- β _M_0.46t_w	0.46	4.5	9	30	2780	0.25	-	1	Yes

RE- β _M_0.92t_w	0.92	4.5	9	30	2780	0.25	-	1	Yes
RE- β _M_1.38t_w	1.38	4.5	9	30	2780	0.25	-	1	Yes
RE- β _M_1.84t_w	1.84	4.5	9	30	2780	0.25	-	1	Yes
RE- β _M_2.30t_w	2.30	4.5	9	30	2780	0.25	-	1	Yes
RE- γ _R_0.46t_w	0.46	9	9	30	2780	0.25	-	1	Yes
RE- γ _R_0.92t_w	0.92	9	9	30	2780	0.25	-	1	Yes
RE- γ _R_1.38t_w	1.38	9	9	30	2780	0.25	-	1	Yes
RE- γ _R_1.84t_w	1.84	9	9	30	2780	0.25	-	1	Yes
RE- γ _R_2.30t_w	2.30	9	9	30	2780	0.25	-	1	Yes
RE- γ _L_0.46t_w	0.46	18	18	30	2780	0.25	-	1	Yes
RE- γ _L_0.92t_w	0.92	18	18	30	2780	0.25	-	1	Yes
RE- γ _L_1.38t_w	1.38	18	18	30	2780	0.25	-	1	Yes
RE- γ _L_1.84t_w	1.84	18	18	30	2780	0.25	-	1	Yes
RE- γ _L_2.30t_w	2.30	18	18	30	2780	0.25	-	1	Yes
RE- γ _M_0.46t_w	0.46	4.5	9	30	2780	0.25	-	1	Yes
RE- γ _M_0.92t_w	0.92	4.5	9	30	2780	0.25	-	1	Yes
RE- γ _M_1.38t_w	1.38	4.5	9	30	2780	0.25	-	1	Yes
RE- γ _M_1.84t_w	1.84	4.5	9	30	2780	0.25	-	1	Yes
RE- γ _M_2.30t_w	2.30	4.5	9	30	2780	0.25	-	1	Yes

Table 6. Naming of virtual test specimens.

3.1.3 Reference Array Simulations

Up to 5% strain, all specimens except for RA_M specimen in the 2-direction exhibited linear elastic behavior. The RA_M specimen in the 2-direction underwent buckling below 5% strain for wall thicknesses of 0.46, 0.92, 1.38 and 1.84 mm. For these specimens, the point at which the curve abruptly changed slope was taken as the limit. Corresponding representative element analyses were done with these new limits in mind. Increasing relative density resulted in an exponential increase in compressive moduli. Specimens with similar relative density, regardless of specimen size, exhibited equal moduli (RA_R_0.46t_w & RA_L_0.92t_w, RA_R_0.92t_w & RA_L_1.84t_w). **In Figure 24, the dashed curves represent the ‘L’ type (large) specimens, the solid curves represent the ‘R’ type (regular) specimens and the diamond-marked curves represent the ‘M’ type specimens. X and Y axes are shown in logarithmic scale.**

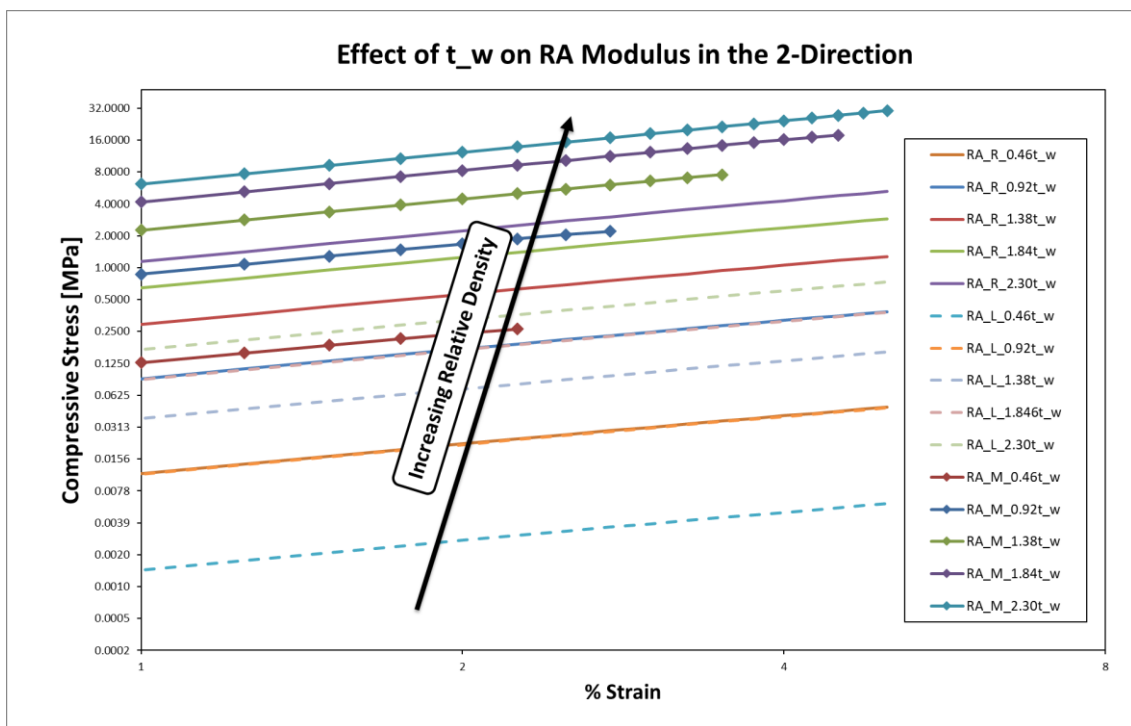
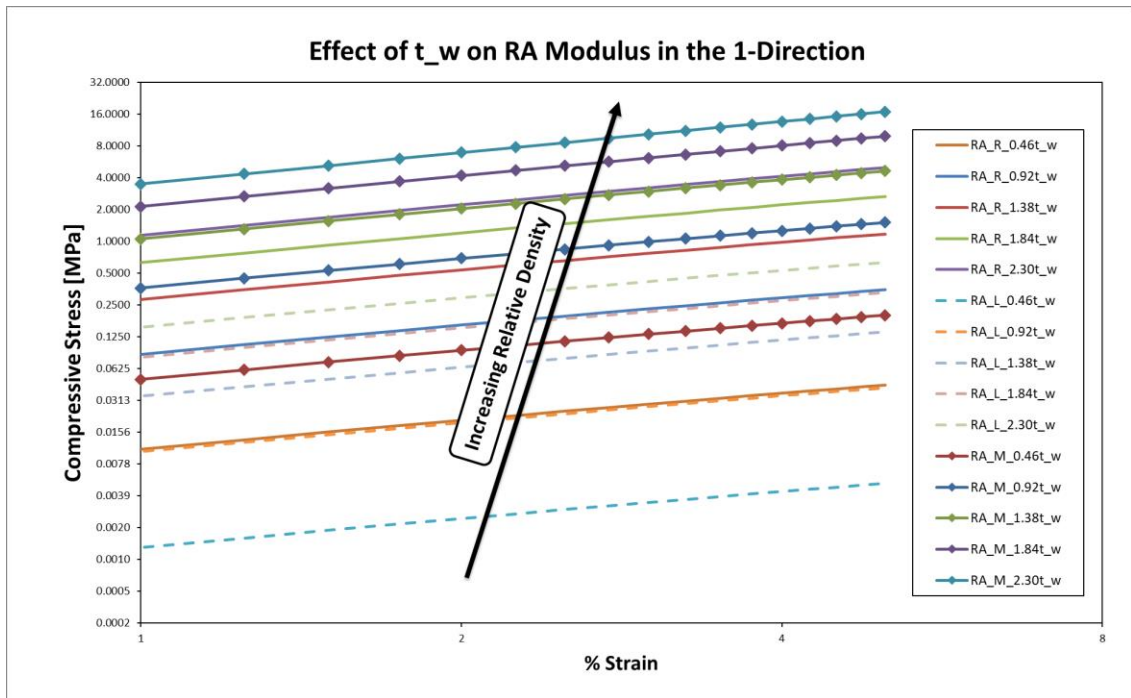


Figure 24. Effect of Cell Wall thickness of RA on the honeycomb elastic modulus under compression in the 1-direction (top) and 2-direction (bottom).

3.1.4 Representative Element Simulations

In figures Figure 25 to Figure 30, the dashed cyan curves, the solid red curves and the solid green curves represent ‘L’, ‘R’ and ‘M’ type specimens, respectively. The faint dashed curves show the parametric analysis of various boundary thicknesses. The black-bound diamond markers show the corresponding representative boundary thickness ‘ t_b^* ’ that causes the representative element to exhibit modulus equivalent to the reference array ‘AR’ for the same wall thickness ‘ t_w ’ and the array stress that they exhibit for 5% contraction.

The shape of the curve, or concavity discussion have been investigated in depth in section 3.3.1.

3.1.4.1 RE- α Simulations

Investigating the array moduli vs representative boundary thickness ‘ t_b^* ’, Re- α specimens exhibited an exponential growth relation for R, L & M specimens in the 1-direction (Figure 25 - middle graph). In the 2-direction, R and L specimens exhibited exponential growth whereas the M specimen exhibited logarithmic growth (Figure 26- middle graph). Re- α _M_1 specimen also exhibited an inflection point that might be attributed to the small sample size of the data pool.

Investigating the relative density vs representative boundary thickness ‘ t_b^* ’, Re- α specimens exhibited an logarithmic growth relation for R, L & M specimens in the 1-direction (Figure 25 - bottom graph). In the 2-direction, R and L specimens exhibited a linear growth relation whereas the M specimen exhibited a logarithmic growth relation (Figure 26- bottom graph).

For the Re- α _M_2.30 t_w _2 specimen, varying the boundary thickness did not result in a convergent solution. This is due to increasing dimension of the specimen and the total displacement not scaling with this increase. For Re- α _M specimens, this analogue was valid in a relative density range of $0 < \frac{\rho^*}{\rho_s} < 0.38$.

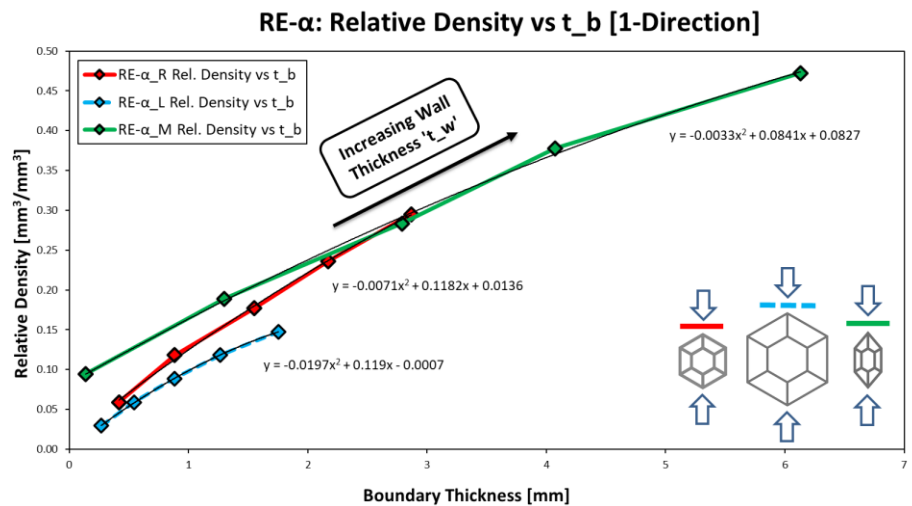
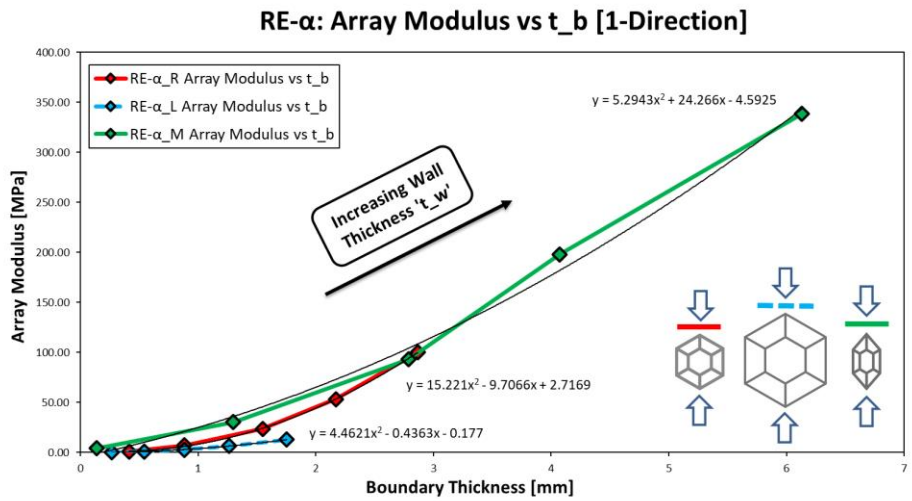
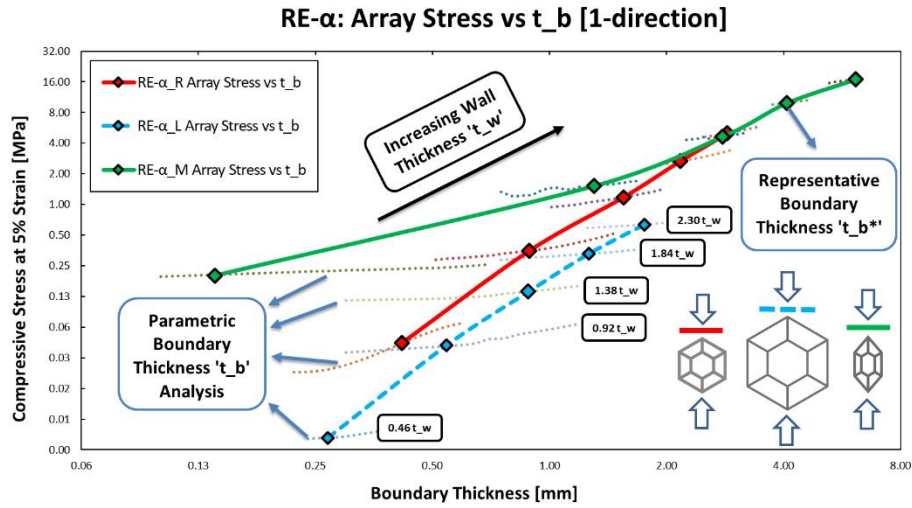


Figure 25. Top: Parametric boundary thickness analysis of RE- α in the 1-direction. Middle: Array modulus vs boundary thickness of RE- α in the 1-direction. Bottom: Relative density vs boundary thickness of RE- α in the 1-direction.

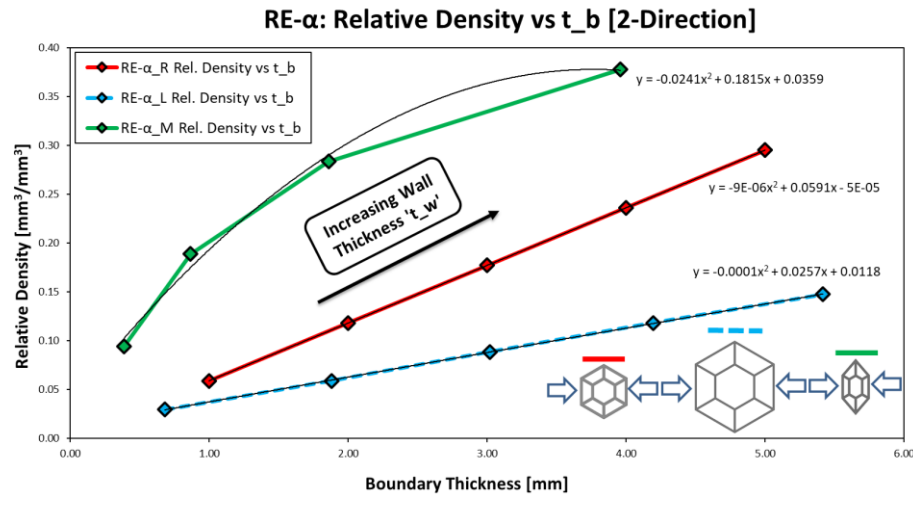
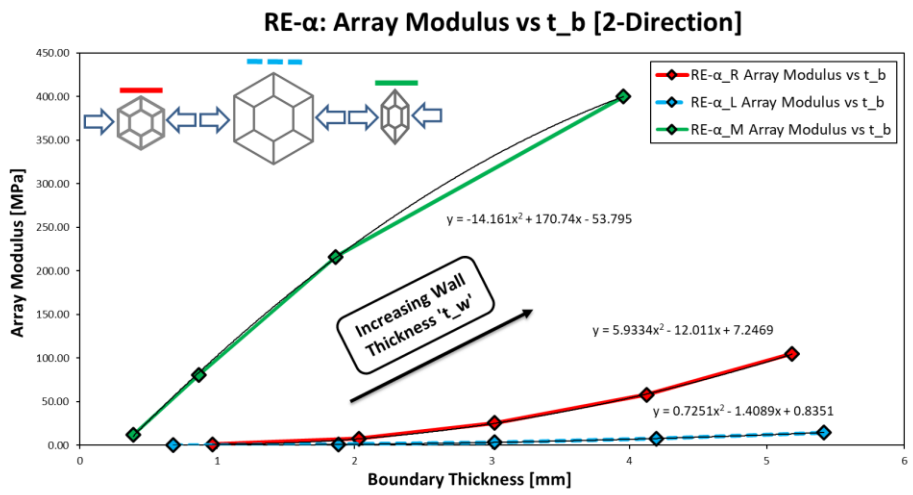
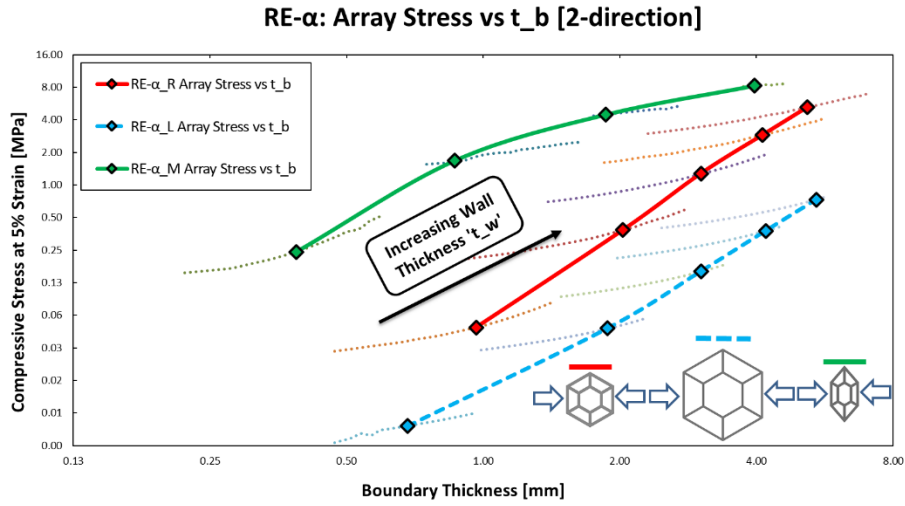


Figure 26. Top: Parametric boundary thickness analysis of RE- α in the 2-direction.
 Middle: Array modulus vs boundary thickness of RE- α in the 2-direction.
 Bottom: Relative density vs boundary thickness of RE- α in the 2-direction.

3.1.4.2 RE- β Simulations

Similar to RE- α specimens, for array moduli vs representative boundary thicknesses behavior, Re- β specimens exhibited an exponential growth relation for R, L & M specimens in the 1-direction and R, L, M specimens in the 2-direction. Re- β _M_2 specimen exhibited 2 inflection points which could be contributed to limited sample size.

For relative density behavior vs representative boundary thicknesses, Re- β specimens exhibited a logarithmic growth relation for R and M specimens and linear relation for L specimen in the 1-direction. R and L specimens exhibited a linear relation in the 2-direction, whereas the M specimen exhibited a logarithmic growth relation. Re- β _M_2 specimen exhibited 1 inflection point which could again be contributed to limited sample size.

For Re- β _M_1.84t_w_1 and Re- β _M_2.30t_w_1 specimens, varying the boundary thickness did not result in a convergent solution. This is due to increasing dimension of the specimen and the total displacement not scaling with this increase. For Re- β _M specimens, this analogue was valid in a relative density range of $0 < \frac{\rho^*}{\rho_s} < 0.28$.

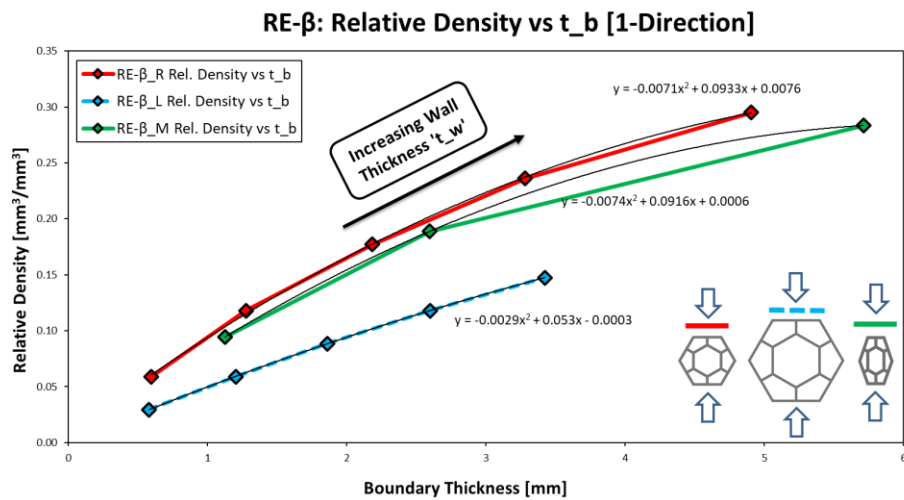
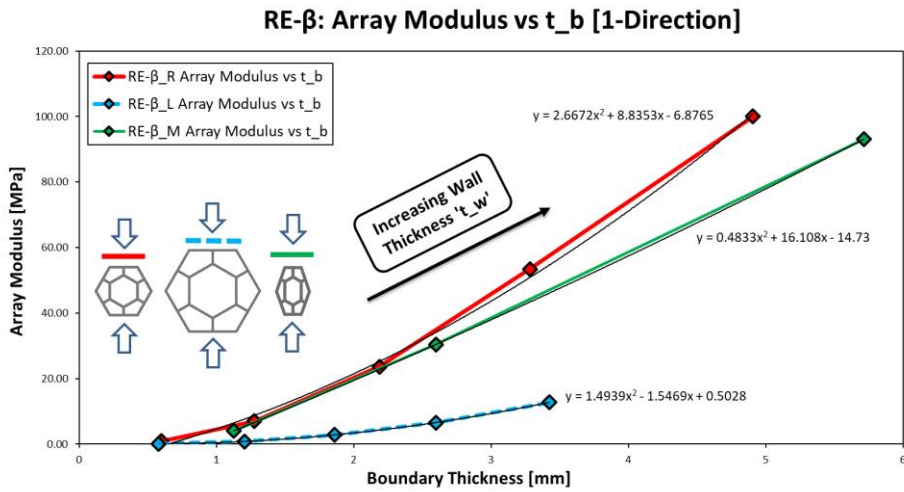
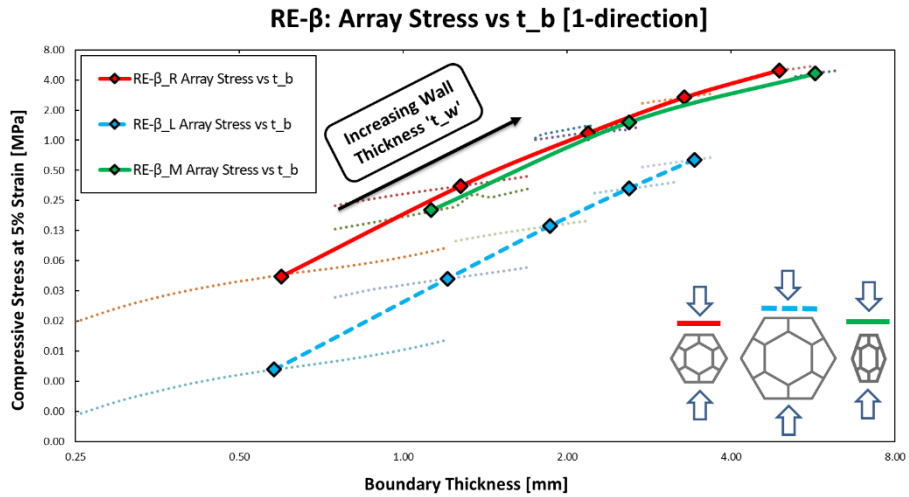


Figure 27. Top: Parametric boundary thickness analysis of RE-β in the 1-direction.
 Middle: Array modulus vs boundary thickness of RE-β in the 1-direction.
 Bottom: Relative density vs boundary thickness of RE-β in the 1-direction.

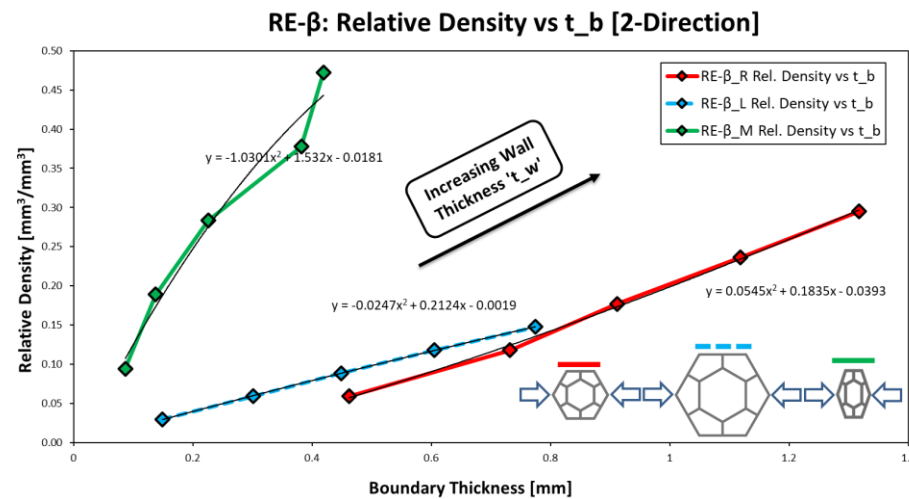
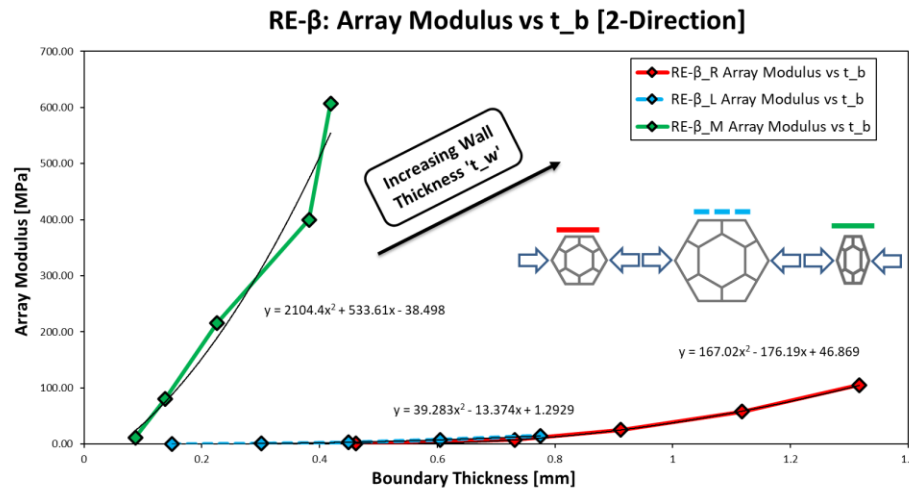
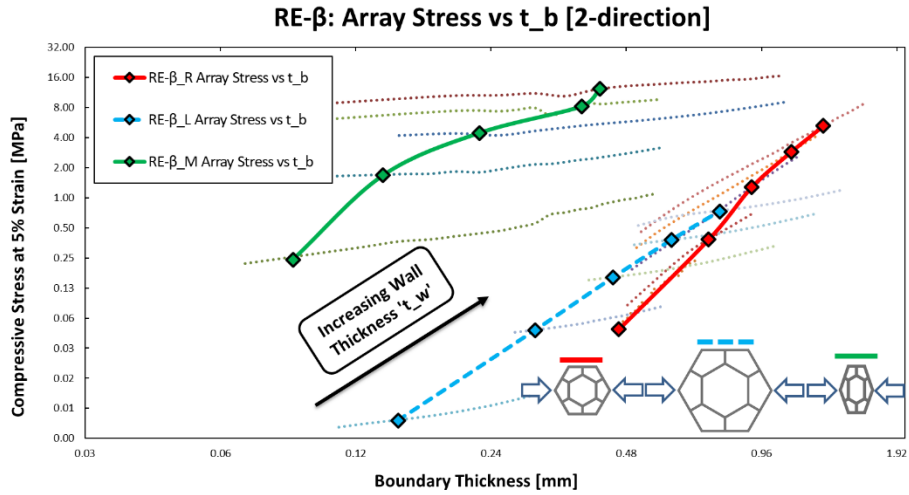


Figure 28. Top: Parametric boundary thickness analysis of RE-β in the 2-direction. Middle: Array modulus vs boundary thickness of RE-β in the 2-direction. Bottom: Relative density vs boundary thickness of RE-β in the 2-direction.

3.1.4.3 RE- γ simulations

For array moduli vs representative boundary thickness behavior, Re- γ specimens exhibited an exponential growth relation for all specimens.

For representative boundary thicknesses vs relative density behavior, Re- γ specimens exhibited a linear relation for all specimens.

This analogue was valid for all attempted relative densities: of $0 < \frac{\rho^*}{\rho_s} < 0.47$

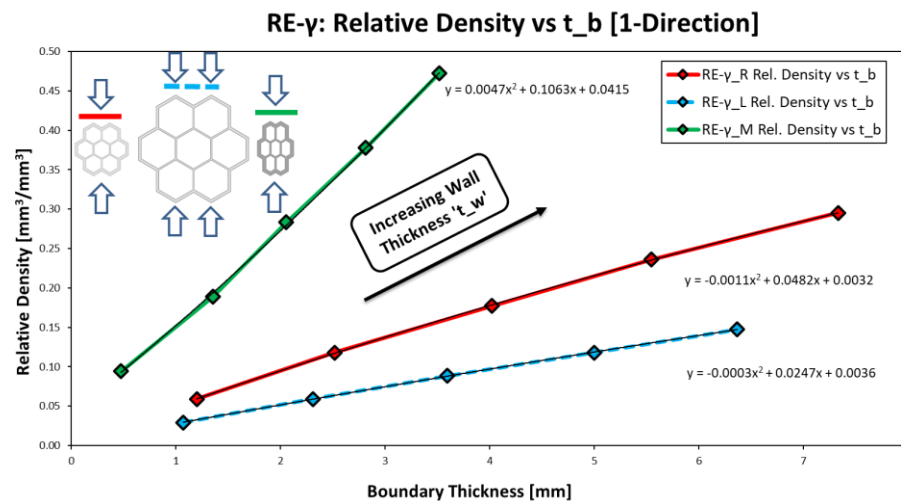
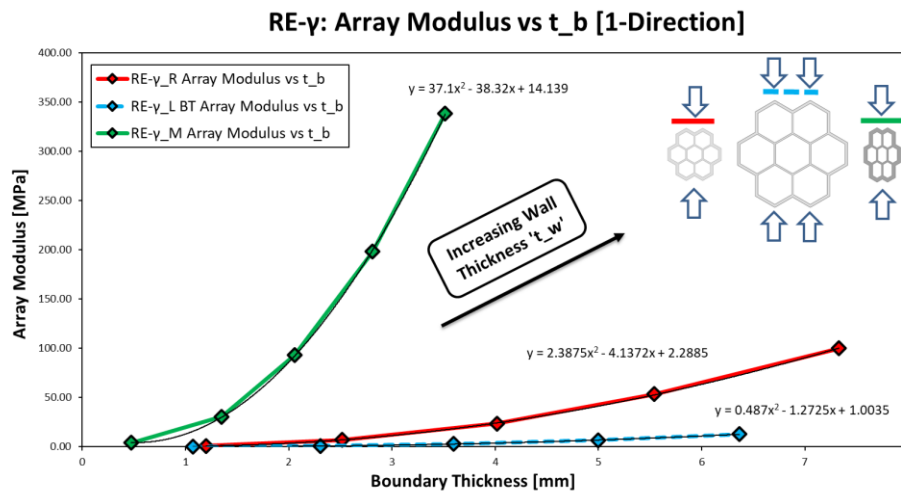
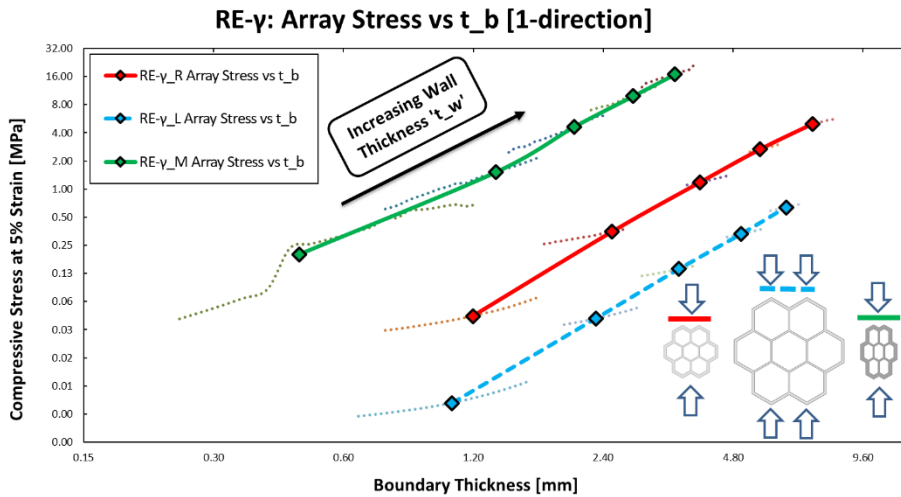


Figure 29. Top: Parametric boundary thickness analysis of RE- γ in the 1-direction.
 Middle: Array modulus vs boundary thickness of RE- γ in the 1-direction.
 Bottom: Relative density vs boundary thickness of RE- γ in the 1-direction.

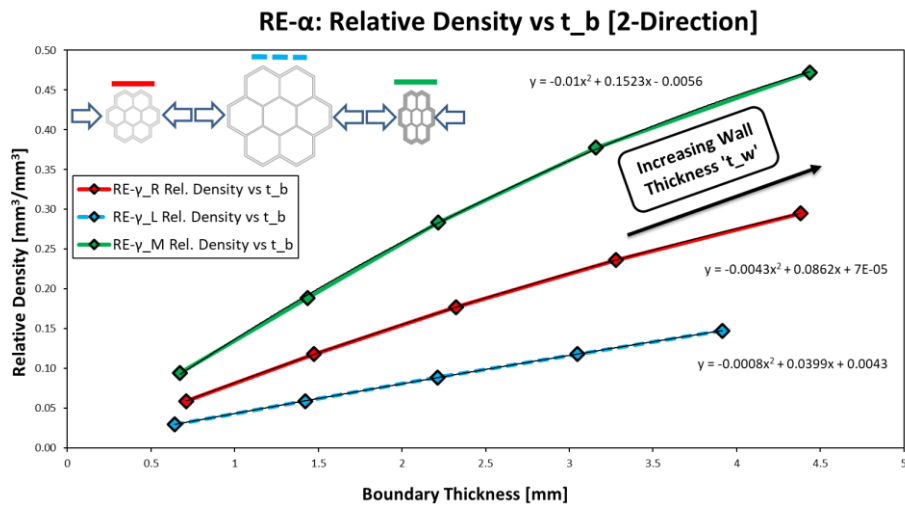
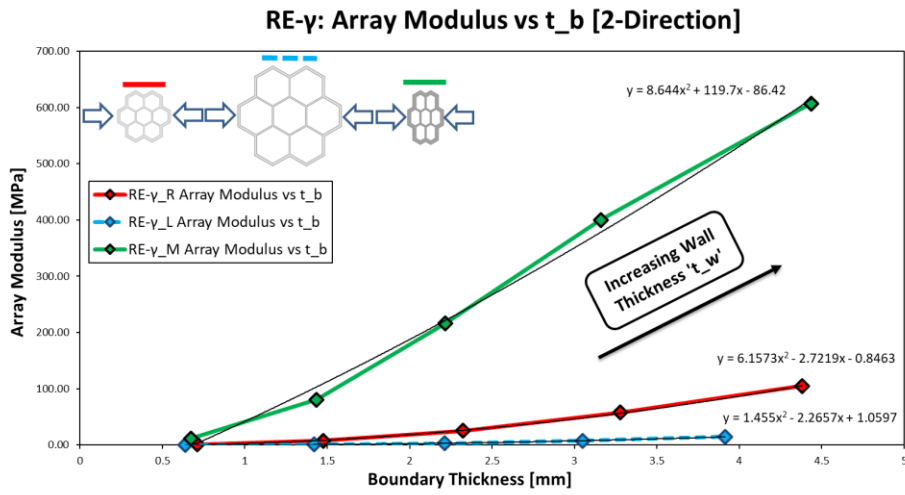
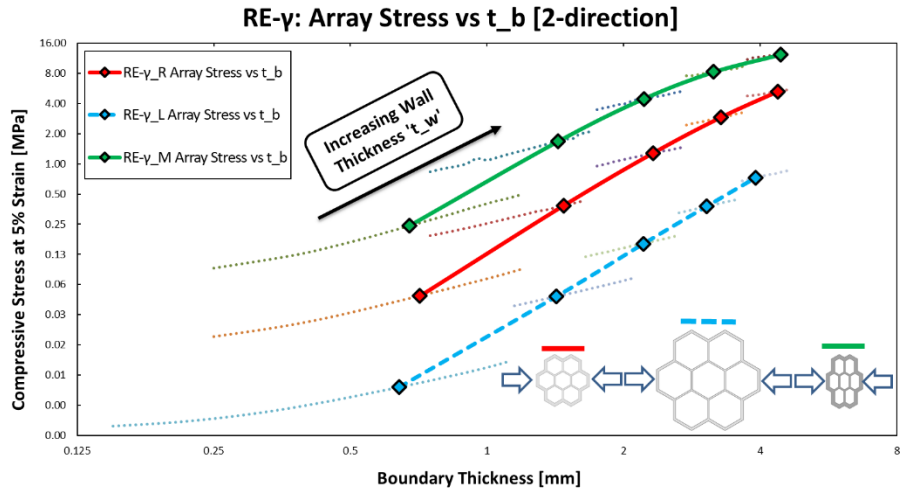


Figure 30. Top: Parametric boundary thickness analysis of RE- γ in the 2-direction.
 Middle: Array modulus vs boundary thickness of RE- γ in the 2-direction.
 Bottom: Relative density vs boundary thickness of RE- γ in the 2-direction.

3.1.5 Representative Ratio for Analogous Specimens

Parametric boundary thickness analysis showed that for every wall thickness value, there exists an appropriate boundary thickness that simulates the larger array ‘RA’. Table 7 & Table 8 outlines these representative boundary thickness (t_{b^*}) along with the modulus of the reference array and how it compares to Ashby/Gibson analytical model (1999) and Malek/Gibson iteration of the same model (2015). Note that the RA FEM results lie in between the two models for all specimens. If the size effect from Onck’s work (2001) is adapted to RA, we see that:

$$\alpha = \frac{W}{D} \quad (\text{Eq. 44})$$

For 1-direction, for values of $W=8H$ and $D=H$, $\alpha=8$.

For 2-direction, for values of $W=10H$ and $D=H$, $\alpha=10$.

Referring back to Table 1 for 1-direction, the $\frac{E^*}{E_{inf}^*}$ value of $\frac{7.45}{\alpha}$ is in good agreement with the data (Table 7, comparing FEA modulus to the analytical models) for relative densities ≥ 0.236 for R-type specimens (such as RA_R_1.84t_w and RA_R_2.30t_w), for all relative densities for L-type specimens, and for relative densities ≤ 0.189 for M-type specimens.

Then, $\frac{E^*}{E_{bulk}^*}$ can be calculated for $\alpha=10$ using the experimental data of L-type specimens in the 2-direction. Averaging values of L-type specimens FEA modulus/Ashby-Gibson modulus:

$$\frac{E^*}{E_{inf}^*} = \frac{10.99}{\alpha} \quad [\text{for } 10 \leq \alpha < 11] \quad (\text{Eq. 45})$$


Thus, for 1-direction, $\frac{E^*}{E_{inf}^*}$ comes out to be 0.931 and for 2-direction $\frac{E^*}{E_{bulk}^*}$ comes out to be 1.099 meaning a 10x10 array simulates an infinite array with less than 10% deviation.

The relative densities (RD) of arrays are calculated from (Eq. 23).

A new concept is introduced as the representative ratio (RR) where:

$$RR = \frac{t_{b^*}}{t_w} \quad (\text{Eq. 46})$$

For specimen subgroups that exhibit $\leq 5\%$ standard error in RR can be considered to have a linear relation between t_{b^*} and t_w . This is shown highlighted in Table 7 and Table 8 as the dark green colored cells.

1 - Direction											
	Wall Thickness [mm]	Relative Density (ρ^*/ρ_s)	FEA Compressive Modulus [MPa]	Ashby/Gibson Analytical Modulus [MPa] 1999	Malek/Gibson Analytical Modulus [MPa] 2015	RE- α Representative Boundary Thickness [mm]	Representative Ratio [Representative Boundary Thickness/ Wall Thickness]	RE- β Representative Boundary Thickness [mm]	Representative Ratio [Representative Boundary Thickness/ Wall Thickness]	RE- γ Representative Boundary Thickness [mm]	Representative Ratio [Representative Boundary Thickness/ Wall Thickness]
RA_R_0.46wt	0.46	0.059	0.87	0.86	0.84	0.42	0.907	0.60	1.300	1.20	2.603
RA_R_0.92wt	0.92	0.118	7.00	6.86	6.42	0.89	0.962	1.28	1.387	2.52	2.735
RA_R_1.38wt	1.38	0.177	23.58	23.17	19.91	1.55	1.122	2.19	1.583	4.02	2.910
RA_R_1.84wt	1.84	0.236	53.42	54.86	41.87	2.17	1.180	3.28	1.784	5.54	3.012
RA_R_2.30wt	2.30	0.295	100.00	107.15	70.54	2.87	1.246	4.91	2.134	7.33	3.187
RA_L_0.46wt	0.46	0.030	0.10	0.11	0.11	0.27	0.585	0.58	1.259	1.07	2.326
RA_L_0.92wt	0.92	0.059	0.83	0.86	0.84	0.54	0.590	1.21	1.311	2.31	2.510
RA_L_1.38wt	1.38	0.089	2.78	2.90	2.79	0.88	0.639	1.86	1.347	3.59	2.603
RA_L_1.84wt	1.84	0.118	6.58	6.86	6.42	1.26	0.686	2.60	1.413	5.00	2.717
RA_L_2.30wt	2.30	0.148	12.74	13.39	12.07	1.76	0.763	3.43	1.490	6.37	2.767
RA_M_0.46wt	0.46	0.094	4.02	4.11	3.85	0.14	0.300	1.13	2.448	0.47	1.030
RA_M_0.92wt	0.92	0.189	30.38	32.92	25.12	1.30	1.413	2.60	2.824	1.35	1.468
RA_M_1.38wt	1.38	0.283	93.09	111.22	61.70	2.79	2.020	5.71	4.139	2.06	1.489
RA_M_1.84wt	1.84	0.378	198.14	263.34	99.21	4.07	2.214	-	-	2.81	1.529
RA_M_2.30wt	2.30	0.472	338.58	514.33	127.43	6.13	2.665	-	-	3.52	1.528

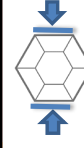
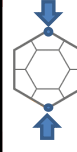
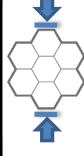


Table 7. Parametric analysis of RA, RE- α , RE- β and RE- γ under compression in the 1-direction. Lower standard error percentages suggest linearity.

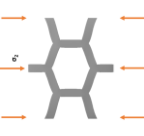
2 - Direction											
	Wall Thickness [mm]	Relative Density (ρ^*/ρ_s)	FEA Compressive Modulus [MPa]	Ashby/Gibson Analytical Modulus [MPa] 1999	Malek/Gibson Analytical Modulus [MPa] 2015	RE- α Representative Boundary Thickness [mm]	Representative Ratio [Representative Boundary Thickness/ Wall Thickness]	RE- β Representative Boundary Thickness [mm]	Representative Ratio [Representative Boundary Thickness/ Wall Thickness]	RE- γ Representative Boundary Thickness [mm]	Representative Ratio [Representative Boundary Thickness/ Wall Thickness]
RA_R_0.46wt	0.46	0.059	0.96	0.86	0.92	0.96	2.097	0.46	1.004	0.71	1.546
RA_R_0.92wt	0.92	0.118	7.63	6.86	7.71	2.03	2.208	0.73	0.796	1.48	1.603
RA_R_1.38wt	1.38	0.177	25.48	23.17	26.30	3.02	2.187	0.91	0.661	2.32	1.683
RA_R_1.84wt	1.84	0.236	57.81	54.86	61.03	4.13	2.242	1.12	0.608	3.28	1.782
RA_R_2.30wt	2.30	0.295	104.87	107.15	113.87	5.19	2.255	1.32	0.573	4.38	1.905
RA_L_0.46wt	0.46	0.030	0.12	0.11	0.11	0.68	1.480	0.15	0.324	0.64	1.391
RA_L_0.92wt	0.92	0.059	0.94	0.86	0.92	1.88	2.044	0.30	0.327	1.42	1.545
RA_L_1.38wt	1.38	0.089	3.18	2.90	3.20	3.02	2.187	0.45	0.325	2.21	1.602
RA_L_1.84wt	1.84	0.118	7.51	6.86	7.71	4.19	2.280	0.61	0.329	3.05	1.657
RA_L_2.30wt	2.30	0.148	14.56	13.39	15.19	5.42	2.355	0.78	0.337	3.91	1.702
RA_M_0.46wt	0.46	0.094	11.77	11.43	12.45	0.39	0.843	0.09	0.189	0.67	1.465
RA_M_0.92wt	0.92	0.189	80.86	91.44	90.50	0.87	0.941	0.14	0.150	1.44	1.561
RA_M_1.38wt	1.38	0.283	216.03	308.93	246.08	1.86	1.347	0.23	0.164	2.22	1.605
RA_M_1.84wt	1.84	0.378	399.99	731.49	448.97	3.96	2.151	0.38	0.208	3.16	1.717
RA_M_2.30wt	2.30	0.472	606.94	1428.69	677.00	-	-	0.42	0.182	4.44	1.929

Table 8. Parametric analysis of RA, RE- α , RE- β and RE- γ under compression in the 2-direction. Lower standard error percentages suggest linearity.

3.2 Mechanical Testing Results

A preliminary experiment was done to test the consistency between mechanical testing and FEM analysis. Same dimensions of RA_R was used, except for the wall thickness, which was 0.74 mm, which was due calibration of the printer (for latter specimens, geometries were printed accurately). Results showed very similar moduli for both the virtual and real-life test.

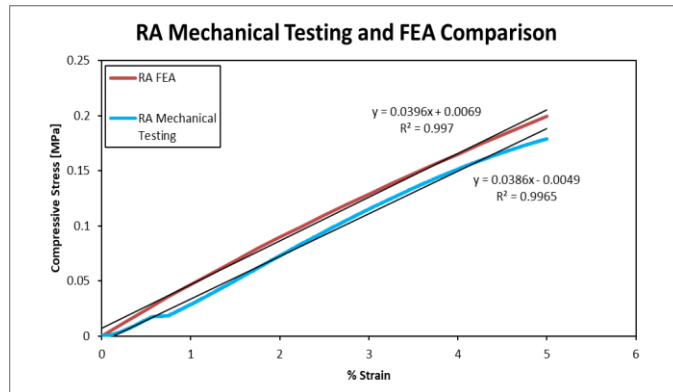


Figure 31. Comparison between FEA analysis and mechanical testing of RA_R specimen.

Taking the perimeter width limitation of an FDM printer into consideration, accurate manufacturing for wall thicknesses < 1.84 mm was unfeasible. 3 sets of specimens were printed with the RA_R_1.84t, RE- α _1.84t, RE- β _1.84t and RE- γ _1.84t geometries using the 3 most common FDM plastics: PLA, PETG and ABS. All three plastics were Esun[®] brand 1.75mm diameter gray colored filaments. Boundary thicknesses were selected from FEM analysis to match the corresponding arrays. Refer to Figure 32, Figure 33 and Figure 34 for the results of these mechanical tests.

Results revealed well matched array and representative element moduli. The fact that t_b^* 's were the same for 3 different materials suggests that the properties of the representative elements are independent of compressive modulus and Poisson's ratio.

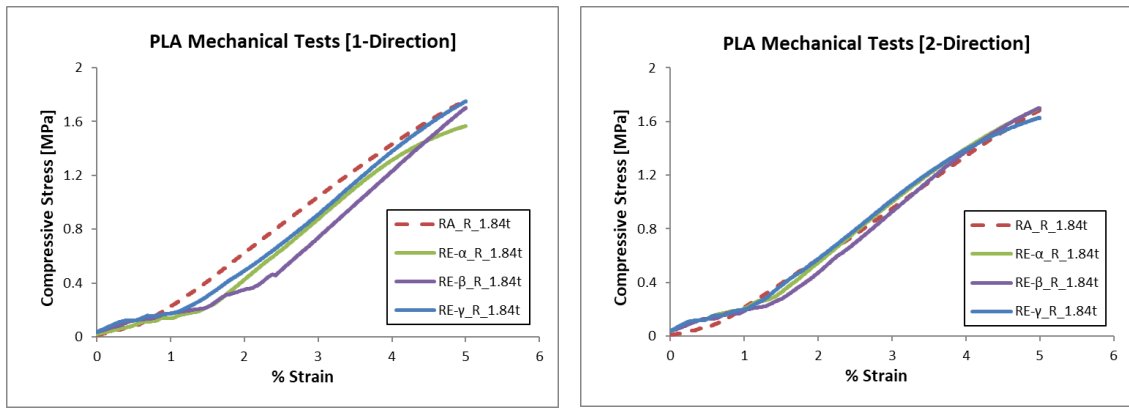


Figure 32. Mechanical test data of PLA array and representative elements in 1-direction (left) and 2-direction (right)

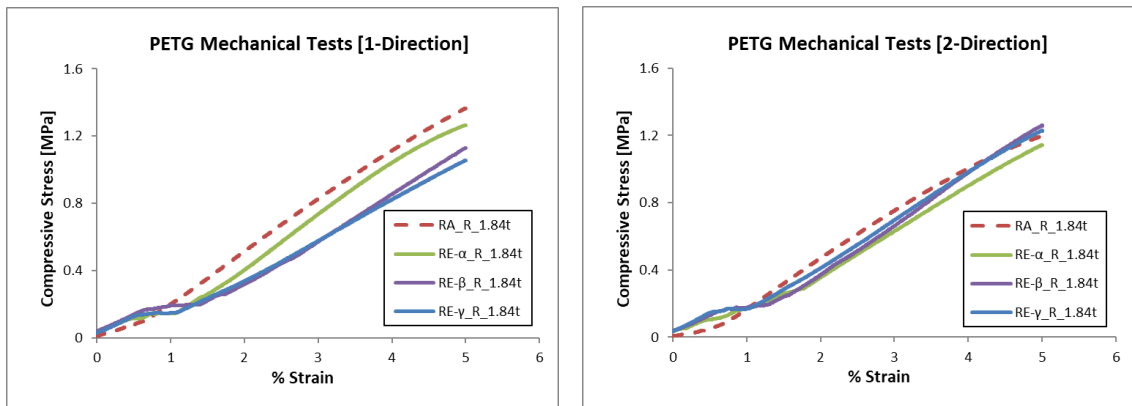


Figure 33. Mechanical test data of PETG array and representative elements in 1-direction (left) and 2-direction (right)

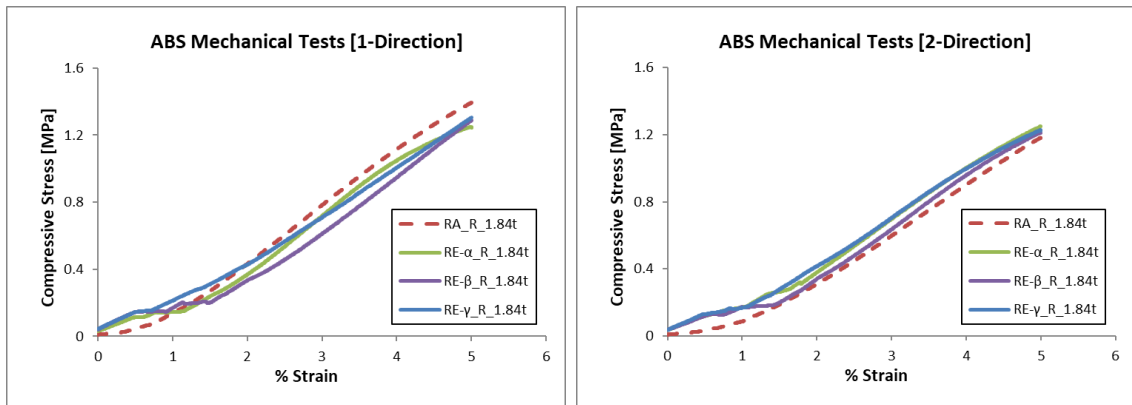


Figure 34. Mechanical test data of ABS array and representative elements in 1-direction (left) and 2-direction (right)

3.3 Choosing the Most Applicable Geometry

3.3.1 Consistency of Response

When choosing the best representative element, a consistency between array modulus vs t_b and relative density vs t_b curve shapes of R, L and M type specimens are desired so that structures are predictive for all aspect ratios of the same geometry. By inspecting the concavity, or the sign of the second derivative of the curves in the middle (AM vs t_b) and bottom (rel. density vs t_b) graphs in figures Figure 25 to Figure 30, we can outline the behaviour of the geometries and how they change with varying honeycomb parameters such as h/l ratio or θ .

For this goal, 2nd degree polynomial trendlines were fitted to array modulus vs t_b and relative density vs t_b curves.

Curves with $f''(x) > \frac{MAX([y])}{MAX([x])} (0.01)$ were considered as concave up (increasing),

Curves with $f''(x) < -\frac{MAX([y])}{MAX([x])} (0.01)$ were considered as concave down (increasing),

Curves with $-\frac{MAX([y])}{MAX([x])} (0.01) \leq f''(x) \leq \frac{MAX([y])}{MAX([x])} (0.01)$ were considered as linear.

Where $MAX(x)$ is the maximum function, $[y]$ is the data set of the y axis and $[x]$ is the data set of the x axis.

In this regard, **RE- α _1, RE- β _1, RE- γ _1 and RE- γ _2 specimen groups retained concavity among all geometries.**

Specimen Type	Array Modulus vs t_b	Relative Density vs t_b	Specimen Type	Array Modulus vs t_b	Relative Density vs t_b	Specimen Type	Array Modulus vs t_b	Relative Density vs t_b
RE- α _R_1	(+)	(-)	RE- β _R_1	(+)	(-)	RE- γ _R_1	(+)	(-)
RE- α _L_1	(+)	(-)	RE- β _L_1	(+)	(-)	RE- γ _L_1	(+)	(-)
RE- α _M_1	(+)	(-)	RE- β _M_1	(+)	(-)	RE- γ _M_1	(+)	(-)
RE- α _R_2	(+)	≈ 0	RE- β _R_2	(+)	(+)	RE- γ _R_2	(+)	(-)
RE- α _L_2	(+)	≈ 0	RE- β _L_2	(+)	(-)	RE- γ _L_2	(+)	(-)
RE- α _M_2	(-)	(-)	RE- β _M_2	(+)	(-)	RE- γ _M_2	(+)	(-)

Table 9. The sign of 2nd derivative of the trendline functions of array modulus vs t_b and relative density vs t_b among all representative elements. A positive 2nd derivative indicates up-increasing concavity, a negative 2nd derivative indicated down-increasing concavity and values close to 0 indicate linear behavior.

3.3.2 Scalability of Response

RE- α _R_0.46t and RE- α _L_0.92t, RE- α _R_0.92t and RE- α _L_1.84t specimen pairs have the same relative density (and therefore l/t) values. Thus, the representative ratio of boundary thickness/wall thickness should be same for these geometries. This will exhibit a region of overlap (Figure 35, Figure 36 and Figure 37) in representative ratio vs relative density curves of R, L and M geometries. **RE- α _2, RE- β _1, RE- γ _1 and RE- γ _2 exhibit this scalability.** The geometries that show discrepancy in this regard are outlined in Table 7 & Table 8 with bold, larger red and bold, larger cyan numbers. Numbers of the same color, in the same RR column should be equal to exhibit scalability.

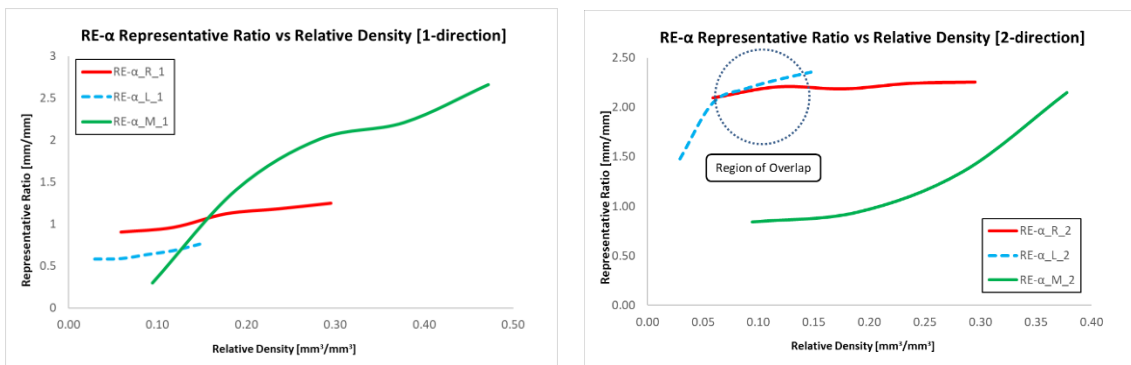


Figure 35. Boundary thickness/wall thickness ratio vs relative density of RE- α specimens.

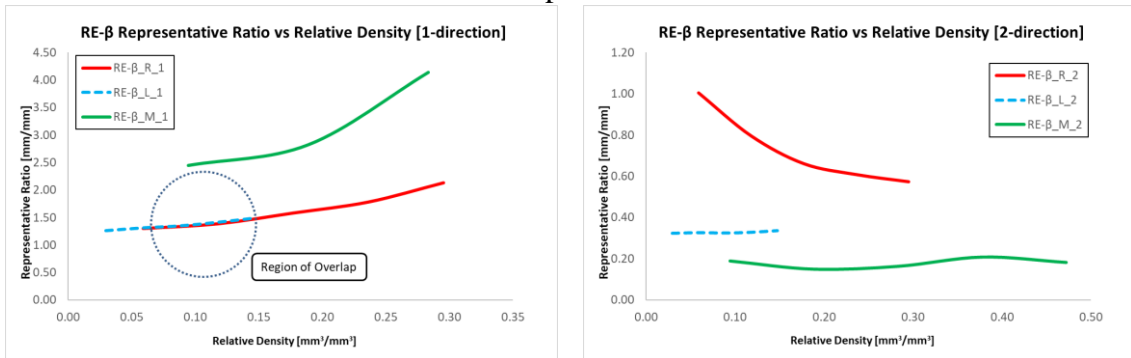


Figure 36. Boundary thickness/wall thickness ratio vs relative density of RE- β specimens.

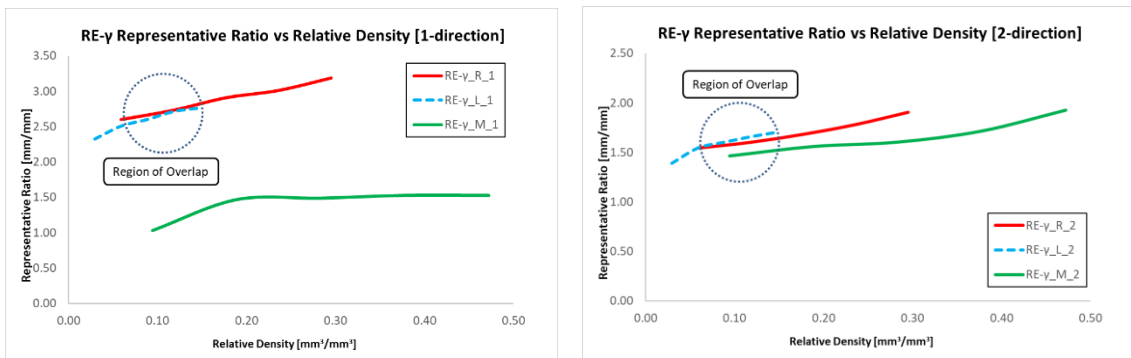


Figure 37. Boundary thickness/wall thickness ratio vs relative density of RE- γ specimens.

3.3.3 Range of Application

Some specimens, regardless of how much the boundary thickens, will not converge to a solution due to having an invariable initial height of the inner bound specimen (Figure 38). **RE- α _1, RE- β _2, RE- γ _1 and RE- γ _2 specimen subgroups exhibited applicable representative boundary thicknesses on all attempted relative densities.**

Specimen Type	Relative Density Range	Specimen Type	Relative Density Range	Specimen Type	Relative Density Range
RE- α _R_1	$0.059 \leq \rho^*/\rho_s \leq 0.295$	RE- β _R_1	$0.059 \leq \rho^*/\rho_s \leq 0.295$	RE- γ _R_1	$0.059 \leq \rho^*/\rho_s \leq 0.295$
RE- α _L_1	$0.030 \leq \rho^*/\rho_s \leq 0.148$	RE- β _L_1	$0.030 \leq \rho^*/\rho_s \leq 0.148$	RE- γ _L_1	$0.030 \leq \rho^*/\rho_s \leq 0.148$
RE- α _M_1	$0.094 \leq \rho^*/\rho_s \leq 0.472$	RE- β _M_1	$0.094 \leq \rho^*/\rho_s \leq 0.283$	RE- γ _M_1	$0.094 \leq \rho^*/\rho_s \leq 0.472$
RE- α _R_2	$0.059 \leq \rho^*/\rho_s \leq 0.295$	RE- β _R_2	$0.059 \leq \rho^*/\rho_s \leq 0.295$	RE- γ _R_2	$0.059 \leq \rho^*/\rho_s \leq 0.295$
RE- α _L_2	$0.030 \leq \rho^*/\rho_s \leq 0.148$	RE- β _L_2	$0.030 \leq \rho^*/\rho_s \leq 0.148$	RE- γ _L_2	$0.030 \leq \rho^*/\rho_s \leq 0.148$
RE- α _M_2	$0.094 \leq \rho^*/\rho_s \leq 0.378$	RE- β _M_2	$0.094 \leq \rho^*/\rho_s \leq 0.472$	RE- γ _M_2	$0.094 \leq \rho^*/\rho_s \leq 0.472$

Table 10. Relative density range of applicability of boundary walls among all representative elements

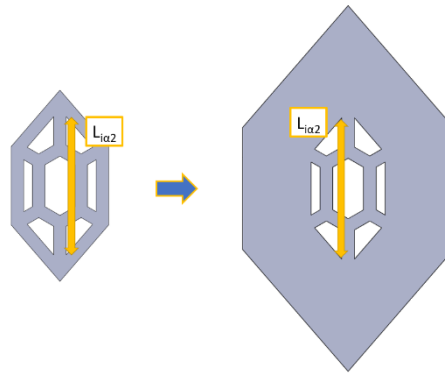


Figure 38. Even at extreme boundary thicknesses, few specimens did not reach the stress of the array exhibited at 5% strain. This is due to initial height of the specimen not scaling with the overall size of the specimen.

3.4 Data Fitting for Determination of b_t for Target Relative Densities

Curve fitting was done on specimens that showed scalability (RE- α _2, RE- β _, RE- γ _1 and RE- γ _2) in MATLAB[®] R2020a Academic. Refer to figures Figure 39 through Figure 42 for trendline & residual plots of these specimens. Coefficients and goodness of fit parameters are outlined in Table 11. Using these plots and equations, it is possible to predict the representative boundary thickness of these geometries. Experimental specimens can then be manufactured and tested under compression to simulate the behaviour of the specific array.

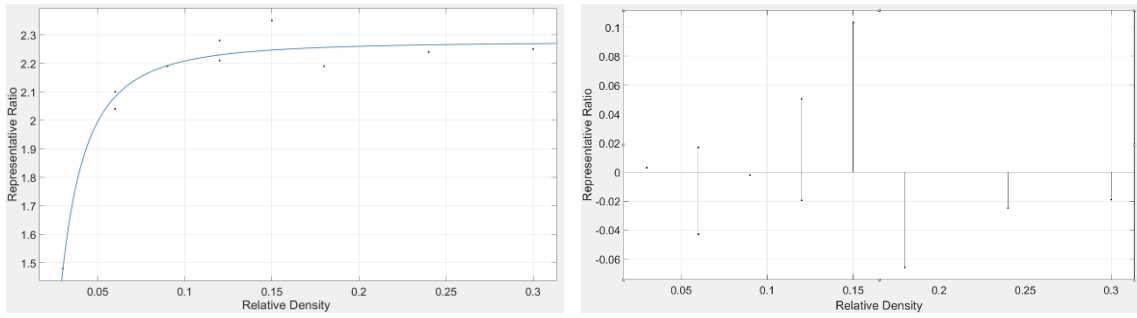


Figure 39. RR vs RD fitting (left) and residuals (right) of RE- α_2

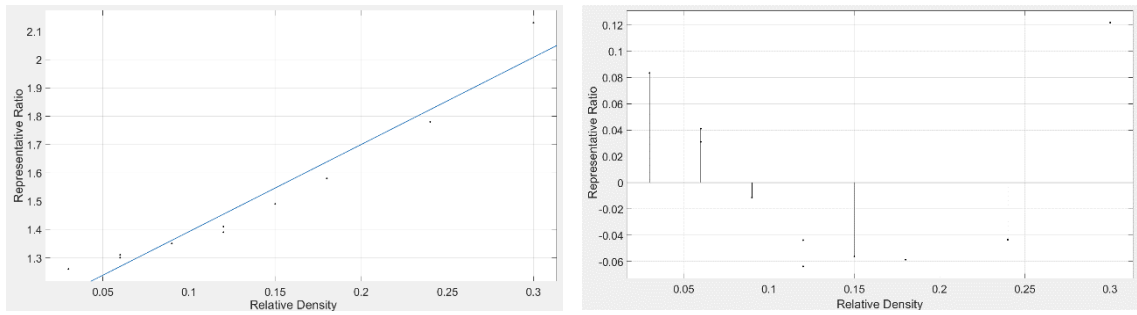


Figure 40. RR vs RD fitting (left) and residuals (right) of RE- β_1 .

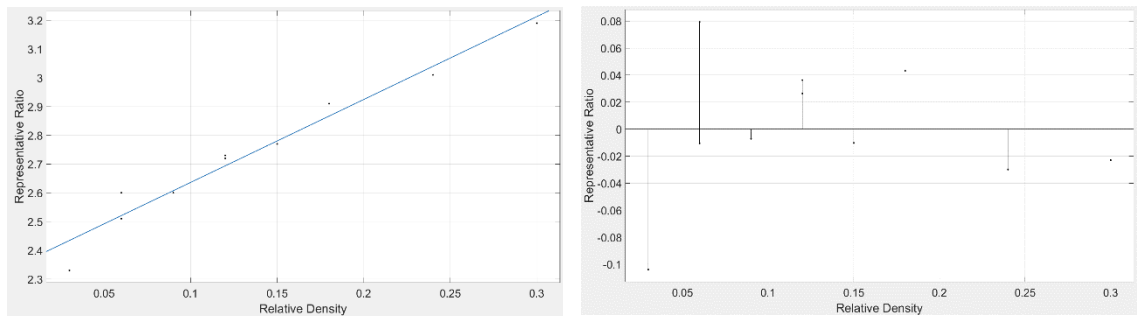


Figure 41. RR vs RD fitting (left) and residuals (right) of RE- γ_1 .

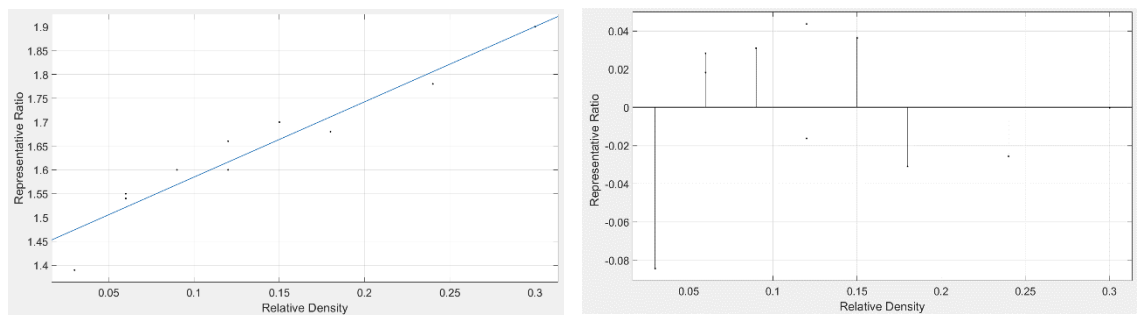


Figure 42. RR vs RD fitting (left) and residuals (right) of RE- γ_2 .

	Fit Equation	p1	p2	p3	SSE	R ²	Adjusted R ²	RMSE
RE- α _2	$(p1)x^{p2}+p3$	-0.00061	-2.048	2.276	0.02109	0.9611	0.95	0.05488
RE- β _1	$(p1)x+p2$	3.08	1.084	-	0.03903	0.9407	0.9333	0.06985
RE- γ _1	$(p1)x+p2$	2.885	2.348	-	0.0227	0.9599	0.9549	0.05327
RE- γ _2	$(p1)x+p2$	1.577	1.427	-	0.01433	0.9189	0.9087	0.04232

Table 11. Fitting parameters and goodness of fit data of RE- α _2, RE- β _1, RE- γ _1 and RE- γ _2

3.4.1 Data Fitting Example Case

When designing a regular honeycomb structure that will be subject to compression in the 2-direction, a relative density of 0.236 is desired by the engineer for its toughness. Using this curve, the representative ratio is:

$$RR = (-0.00061)(0.236)^{-2.048} + 2.276 = \mathbf{2.26}$$

Using Equation 24 and a chosen l length of 9mm:

$$0.236 = \frac{2}{\sqrt{3}} \frac{t}{9}$$

$$t = \mathbf{1.84}$$

The engineer can manufacture a RE- α type specimen with $h = l = 9$ mm, $t_w = \mathbf{1.84}$ mm and $t_b^* = (2.26)(1.84) = \mathbf{4.15}$ mm and test it under compression to infer the compressive response of the structure in 2-direction. This is in fact, one of the mechanical test cases outlined in this work.

3.5 Future Work

Representative element approach should be tested in shear to accompany the compressive response in 1 and 2-directions. The geometries should be diversified to include more irregular shapes such as auxetic or chiral honeycombs. Example representative elements are shown in Figure 43. Hexagonal array tests should be replicated with anisotropic materials such as fiber reinforced composites to see if the reference element boundary relations hold.

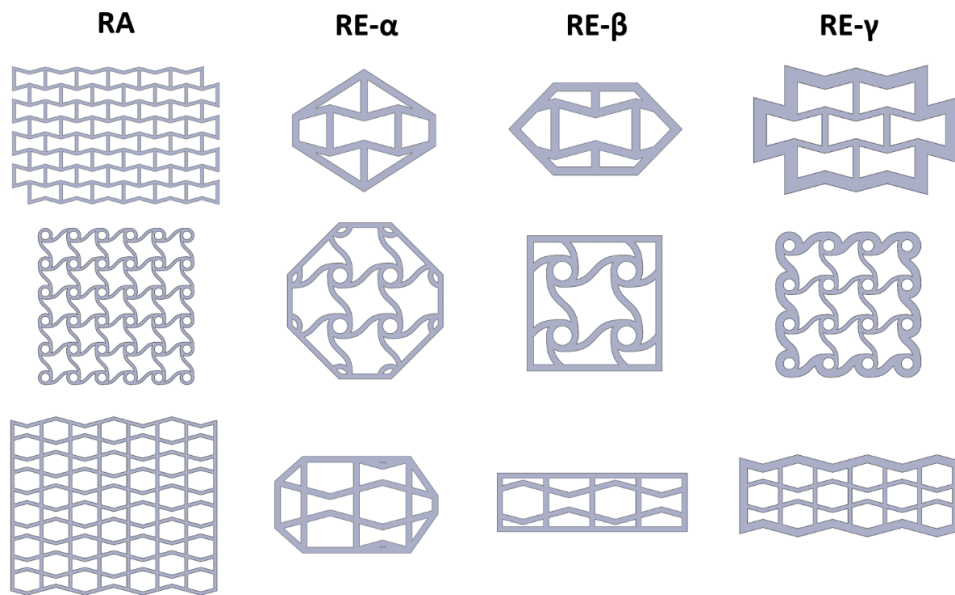


Figure 43. Applying the representative element approach to re-entrant (top row), tetra-chiral (middle row) and hybrid (bottom row) honeycombs.

4 Conclusion

Material constants were obtained through mechanical testing of 3D printed plastic. Using these material constants, parametric finite element analyses were done on preliminary representative geometries theorised to simulate the elastic response of hexagonal honeycombs.

All representative element types were able to simulate the corresponding larger array. However, among 3 element types, only RE- γ was consistent in shape, scalability, and range among regular, scaled up, and irregular geometries. For hexagonal honeycombs, a unit cell surrounded by its immediate neighbors and a parametrized outer shell can work as an analogue for prediction of larger arrays. For analysis in solely 1-direction, the approach of RE- β (bounding the unit cell with vertices on neighbouring cell centers) was valid. For analysis in solely 2-direction, the approach of RE- α (bounding the unit cell with vertices on neighbouring joints) was valid.

Due to size effect, the representative boundary thicknesses will vary when simulating different size and aspect ratio arrays. However, the modulus of the 10x10 array was within 10% deviation from the modulus of an infinite array with the same geometric parameters, making it a decent size array for laying this framework.

Mechanical tests confirmed that for RE- α _R, RE- β _R and RE- γ _R, the representative boundary thicknesses simulated the reference arrays successfully. The representative elements exhibited moduli very similar to their respective reference arrays. The variation of material used suggested that t_b^* prediction is independent of material properties.

This approach of using experimental analogues can be used where novel array designs are proposed, but their properties cannot be determined by the size limitations of either the manufacturing or testing equipment, or cost limitations as representative elements use much less material in comparison.

5 References

- [1] F. López Jiménez and N. Triantafyllidis, “Buckling of rectangular and hexagonal honeycomb under combined axial compression and transverse shear Dedicated to Prof. S. Kyriakides on the occasion of his 60th birthday.,” *Int. J. Solids Struct.*, vol. 50, no. 24, pp. 3934–3946, 2013, doi: 10.1016/j.ijsolstr.2013.08.001.
- [2] S. Duan, Y. Tao, H. Lei, W. Wen, J. Liang, and D. Fang, “Enhanced out-of-plane compressive strength and energy absorption of 3D printed square and hexagonal honeycombs with variable-thickness cell edges,” *Extrem. Mech. Lett.*, vol. 18, pp. 9–18, 2018, doi: 10.1016/j.eml.2017.09.016.
- [3] M. K. Khan, T. Baig, and S. Mirza, “Experimental investigation of in-plane and out-of-plane crushing of aluminum honeycomb,” *Mater. Sci. Eng. A*, vol. 539, pp. 135–142, 2012, doi: 10.1016/j.msea.2012.01.070.
- [4] S. Xu, J. H. Beynon, D. Ruan, and G. Lu, “Experimental study of the out-of-plane dynamic compression of hexagonal honeycombs,” *Compos. Struct.*, vol. 94, no. 8, pp. 2326–2336, 2012, doi: 10.1016/j.compstruct.2012.02.024.
- [5] R. Wang and J. Wang, “Modeling of honeycombs with laminated composite cell walls,” *Compos. Struct.*, vol. 184, no. July 2016, pp. 191–197, 2018, doi: 10.1016/j.compstruct.2017.09.054.
- [6] S. Sorohan, D. M. Constantinescu, M. Sandu, and A. G. Sandu, “On the homogenization of hexagonal honeycombs under axial and shear loading. Part II: Comparison of free skin and rigid skin effects on effective core properties,” *Mech. Mater.*, vol. 119, pp. 92–108, 2018, doi: 10.1016/j.mechmat.2017.09.004.
- [7] F. Côté, V. S. Deshpande, N. A. Fleck, and A. G. Evans, “The out-of-plane compressive behavior of metallic honeycombs,” *Mater. Sci. Eng. A*, vol. 380, no. 1, pp. 272–280, 2004, doi: 10.1016/j.msea.2004.03.051.
- [8] J. Zhang and M. F. Ashby, “The out-of-plane properties of honeycombs,” *Int. J. Mech. Sci.*, vol. 34, no. 6, pp. 475–489, 1992, doi: 10.1016/0020-7403(92)90013-7.
- [9] D. H. Chen, “Bending deformation of honeycomb consisting of regular hexagonal

- cells," *Compos. Struct.*, vol. 93, no. 2, pp. 736–746, 2011, doi: 10.1016/j.compstruct.2010.08.006.
- [10] S. D. Papka and S. Kyriakides, "In-plane compressive response and crushing of honeycomb," *J. Mech. Phys. Solids*, vol. 42, no. 10, pp. 1499–1532, 1994, doi: 10.1016/0022-5096(94)90085-X.
- [11] S. D. Papka and S. Kyriakides, "In-plane crushing of a polycarbonate honeycomb," *Int. J. Solids Struct.*, vol. 35, no. 3–4, pp. 239–267, 1998, doi: 10.1016/S0020-7683(97)00062-0.
- [12] A. Hömig and W. J. Stronge, "In-plane dynamic crushing of honeycomb. Part I: Crush band initiation and wave trapping," *Int. J. Mech. Sci.*, vol. 44, no. 8, pp. 1665–1696, 2002, doi: 10.1016/S0020-7403(02)00060-7.
- [13] Q. Chen and N. M. Pugno, "In-plane elastic buckling of hierarchical honeycomb materials," *Eur. J. Mech. A/Solids*, vol. 34, pp. 120–129, 2012, doi: 10.1016/j.euromechsol.2011.12.003.
- [14] J. Huang, Q. Zhang, F. Scarpa, Y. Liu, and J. Leng, "In-plane elasticity of a novel auxetic honeycomb design," *Compos. Part B Eng.*, vol. 110, pp. 72–82, 2017, doi: 10.1016/j.compositesb.2016.11.011.
- [15] A.-J. Wang and D. L. McDowell, "In-Plane Stiffness and Yield Strength of Periodic Metal Honeycombs," *J. Eng. Mater. Technol.*, vol. 126, no. 2, p. 137, 2004, doi: 10.1115/1.1646165.
- [16] I. G. Masters and K. E. Evans, "Models for the elastic deformation of honeycombs," *Compos. Struct.*, vol. 35, no. 4, pp. 403–422, 1996, doi: 10.1016/S0263-8223(96)00054-2.
- [17] F. Scarpa, P. Panayiotou, and G. Tomlinson, "Numerical and experimental uniaxial loading on in-plane auxetic honeycombs," *J. Strain Anal. Eng. Des.*, vol. 35, no. 5, pp. 383–388, 2000, doi: 10.1243/0309324001514152.
- [18] C. M. Taylor, C. W. Smith, W. Miller, and K. E. Evans, "The effects of hierarchy on the in-plane elastic properties of honeycombs," *Int. J. Solids Struct.*, vol. 48, no.

- 9, pp. 1330–1339, 2011, doi: 10.1016/j.ijsolstr.2011.01.017.
- [19] H. X. Zhu and N. J. Mills, “The in-plane non-linear compression of regular honeycombs,” *Int. J. Solids Struct.*, vol. 37, no. 13, pp. 1931–1949, 2000, doi: 10.1016/S0020-7683(98)00324-2.
- [20] C. Qiu, Z. Guan, S. Jiang, and Z. Li, “A method of determining effective elastic properties of honeycomb cores based on equal strain energy,” *Chinese J. Aeronaut.*, vol. 30, no. 2, pp. 766–779, 2017, doi: 10.1016/j.cja.2017.02.016.
- [21] S. Balawi and J. L. Abot, “A refined model for the effective in-plane elastic moduli of hexagonal honeycombs,” *Compos. Struct.*, vol. 84, no. 2, pp. 147–158, 2008, doi: 10.1016/j.compstruct.2007.07.009.
- [22] J. Zhang and M. F. Ashby, “Buckling of honeycombs under in-plane biaxial stresses,” *Int. J. Mech. Sci.*, vol. 34, no. 6, pp. 491–509, 1992, doi: 10.1016/0020-7403(92)90014-8.
- [23] F. Scarpa, S. Blain, T. Lew, D. Perrott, M. Ruzzene, and J. R. Yates, “Elastic buckling of hexagonal chiral cell honeycombs,” *Compos. Part A Appl. Sci. Manuf.*, vol. 38, no. 2, pp. 280–289, 2007, doi: 10.1016/j.compositesa.2006.04.007.
- [24] D. Mousanezhad, B. Haghpanah, R. Ghosh, A. M. Hamouda, H. Nayeb-Hashemi, and A. Vaziri, “Elastic properties of chiral, anti-chiral, and hierarchical honeycombs: A simple energy-based approach,” *Theor. Appl. Mech. Lett.*, vol. 6, no. 2, pp. 81–96, 2016, doi: 10.1016/j.taml.2016.02.004.
- [25] Y. Chen, R. Das, and M. Battley, “Experimental study on in-plane compressive response of irregular honeycombs,” *J. Compos. Mater.*, vol. 52, no. 8, pp. 1121–1135, 2018, doi: 10.1177/0021998317749964.
- [26] S. D. Papka and S. Kyriakides, “Experiments and full-scale numerical simulations of in-plane crushing of a honeycomb,” *Acta Mater.*, vol. 46, no. 8, pp. 2765–2776, 1998, doi: 10.1016/S1359-6454(97)00453-9.
- [27] Y. Sun and N. M. Pugno, “In plane stiffness of multifunctional hierarchical

- honeycombs with negative Poisson's ratio sub-structures," *Compos. Struct.*, vol. 106, pp. 681–689, 2013, doi: 10.1016/j.compstruct.2013.05.008.
- [28] L. J. Gibson and M. F. Ashby, *Cellular solids*, 2nd ed., vol. 1, no. 1. 1989.
- [29] PATEL and M. R., "Structure features and mechanical properties of rigid cellular plastics," *J. Mater.*, vol. 5, pp. 909–932, 1970, Accessed: Aug. 08, 2020. [Online]. Available: <http://ci.nii.ac.jp/naid/10014657523/en/>.
- [30] F. K. Abd El-Sayed, R. Jones, and I. W. Burgess, "A theoretical approach to the deformation of honeycomb based composite materials," *Composites*, vol. 10, no. 4, pp. 209–214, 1979, doi: [https://doi.org/10.1016/0010-4361\(79\)90021-1](https://doi.org/10.1016/0010-4361(79)90021-1).
- [31] L. J. Gibson and M. F. Ashby, "The mechanics cellular materials of three-dimensional cellular materials," *Proc. R. Soc. L.*, vol. A382, pp. 43–59, 1982.
- [32] S. Malek and L. Gibson, "Effective elastic properties of periodic hexagonal honeycombs," *Mech. Mater.*, vol. 91, no. P1, pp. 226–240, 2015, doi: 10.1016/j.mechmat.2015.07.008.
- [33] P. R. Onck, E. W. Andrews, and L. J. Gibson, "Size effects in ductile cellular solids. Part I: modeling," *Int. J. Mech. Sci.*, vol. 43, no. 3, pp. 681–699, 2001, doi: [https://doi.org/10.1016/S0020-7403\(00\)00042-4](https://doi.org/10.1016/S0020-7403(00)00042-4).
- [34] E. W. Andrews, G. Gioux, P. Onck, and L. J. Gibson, "Size effects in ductile cellular solids. Part II: experimental results," *Int. J. Mech. Sci.*, vol. 43, no. 3, pp. 701–713, 2001, doi: [https://doi.org/10.1016/S0020-7403\(00\)00043-6](https://doi.org/10.1016/S0020-7403(00)00043-6).
- [35] C. Tekog̃lu, L. J. Gibson, T. Pardoen, and P. R. Onck, "Size effects in foams: Experiments and modeling," *Prog. Mater. Sci.*, vol. 56, no. 2, pp. 109–138, 2011, doi: <https://doi.org/10.1016/j.pmatsci.2010.06.001>.
- [36] L. Yang, "A study about size effects of 3D periodic cellular structures," pp. 2181–2193, 2016.
- [37] D. Bhate, "Size Effects in the Characterization of Cellular Materials," 2018. <https://3dxresearch.com/2018/02/06/size-effects-in-the-characterization-of-cellular-materials/> (accessed Aug. 13, 2020).

- [38] Y. Zhao, M. Ge, and W. Ma, "The effective in-plane elastic properties of hexagonal honeycombs with consideration for geometric nonlinearity," *Compos. Struct.*, vol. 234, no. October 2019, p. 111749, 2020, doi: 10.1016/j.compstruct.2019.111749.
- [39] Y. Chen and H. Hu, "In-plane elasticity of regular hexagonal honeycombs with three different joints: A comparative study," *Mech. Mater.*, vol. 148, no. June, p. 103496, 2020, doi: 10.1016/j.mechmat.2020.103496.
- [40] R. T. L. Ferreira, I. C. Amatte, T. A. Dutra, and D. Bürger, "Experimental characterization and micrography of 3D printed PLA and PLA reinforced with short carbon fibers," *Compos. Part B Eng.*, vol. 124, no. September, pp. 88–100, 2017, doi: 10.1016/j.compositesb.2017.05.013.
- [41] J. Jose and S. Perez, "Characterization of PLA and design of a 3D printed wing," 2018.